Molecular Therapy
Original Article

TV-circRGPD6 Nanoparticle Suppresses Breast Cancer Stem Cell-Mediated Metastasis via the miR-26b/YAF2 Axis

Xiaoti Lin,[1,2,5] Weiyu Chen,[3,5] Fengqin Wei,[4,5] and Xiaoming Xie[1]

[1]Department of Breast Oncology, State Key Laboratory of Oncology in South China, Sun Yat-sen University Cancer Center, Collaborative Innovation Center for Cancer Medicine, Guangzhou 510060, China; [2]Department of Breast, Fujian Provincial Maternity and Children's Hospital of Fujian Medical University, Fuzhou 350000, China; [3]Department of Physiology, Zhongshan Medical School, Sun Yat-sen University, Guangzhou 510060, China; [4]Department of Emergency, Fujian Provincial 2nd People's Hospital, Affiliated Hospital of Fujian University of Traditional Chinese Medicine, Fuzhou 350000, China

Metastatic tumor is a major contributor to death caused by breast cancer. However, effective and targeted therapy for metastatic breast cancer remains to be developed. Initially, we exploited a feasible biological rationale of the association between metastatic status and tumor-initiating properties in metastatic breast cancer stem cells (BCSCs). Further, we explored that circular RNA RANBP2-like and GRIP domain-containing protein 6 (circRGPD6) regulates the maintenance of stem cell-like characteristics of BCSCs. Targeted expression of circRGPD6 via human telomerase reverse transcriptase (hTERT) promoter-driven VP16-GAL4-woodchuck hepatitis virus posttranscriptional regulatory element (WPRE)-integrated systemic amplifier delivery composite vector (TV-circRGPD6) significantly inhibited expression of stem-cell marker CD44 and increased expression of the DNA damage marker p-H2AX. Furthermore, we determined TV-circRGPD6, alone or synergized with docetaxel, displays significant therapeutic responses on metastatic BCSCs. Mechanistic analyses exploited that TV-circRGPD6 suppresses BCSC-mediated metastasis via the microRNA (miR)-26b/YAF2 axis. Clinically, for the first time, we observed that expressions of circRGPD6 and YAF2 predict a favorable prognosis in patients with breast cancer, whereas expression of miR-26b is an unfavorable prognostic factor. Overall, we have developed a TV-circRGPD6 nanoparticle that selectively expresses circRGPD6 in metastatic BCSCs to eradicate breast cancer metastasis, therefore providing a novel avenue to treat breast cancers.

INTRODUCTION

Breast cancer (BC) is the most common type of diagnosed and lethal cancer in women; moreover, metastatic tumor contributes to the major deaths caused by BC.[1,2] Metastasis is a process by which a cancer cell spread to a different part of the body from where it started. Further, metastatic cancer cells are derived from especially aggressive subpopulations of the primary tumor and further develop to higher-grade malignant tumors after dissemination to distant places. Furthermore, metastatic cancer cells also have abundant tumor-initiating properties. All of these characteristics have heightened the therapy resistance of the metastatic tumor.[3,4] Accordingly, effective therapy that specifically combats metastasis remains limited.

Recent studies have revealed that control of non-cancer stem cells (non-CSCs) switching to CSCs and regulation of stem-like properties of cancer cells are appealing strategies to prevent progression of tumors toward the metastatic stage.[5,6] However, the biological mechanism of constructing the association between metastatic model and stemness characteristics remains a major obstacle.[3,6] Therefore, researchers are in desperate need of a model to investigate metastasis tumors, stem cell-like characteristics, and tumor-initiating properties in the course of metastatic CSCs. In previous investigations, our group has successfully generated four long-term-cultured breast CSCs (BCSCs), including MDA-MB-231.SC, MCF-7.SC, XM322, and XM607. These BCSCs present prolonged maintenance over 20 passages and keep their tumor-initiating properties.[7,8] As a result, prolonged maintenance of BCSCs is an ideal tool to exploit the direct link between BCSCs and metastasis during cancer progression.

Epithelial-mesenchymal transition (EMT) is a very important process in metastasis. In the process of EMT, differentiated epithelial cancer cells reverse to an undifferentiated state with expressing markers of a stem cell niche and also holding stem cell-like characteristics.[9] Under this circumstance, non-CSCs switch to CSCs by activating their unique abilities of self-renewal, wide differentiation potentials, and resistance to conventional therapy. However, a novel treatment

---

Received 4 April 2020; accepted 1 September 2020;
https://doi.org/10.1016/j.ymthe.2020.09.005.

[5]These authors contributed equally to this work.

Correspondence: Xiaoming Xie, Department of Breast Oncology, State Key Laboratory of Oncology in South China, Sun Yat-Sen University Cancer Center, Collaborative Innovation Center for Cancer Medicine, 651 East Dong Feng Road, Guangzhou 510060, China.
E-mail: xiexm@sysucc.org.cn
Correspondence: Xiaoti Lin, Department of Breast Oncology, State Key Laboratory of Oncology in South China, Sun Yat-Sen University Cancer Center, Collaborative Innovation Center for Cancer Medicine, 651 East Dong Feng Road, Guangzhou 510060, China.
E-mail: linxt3@mail2.sysu.edu.cn

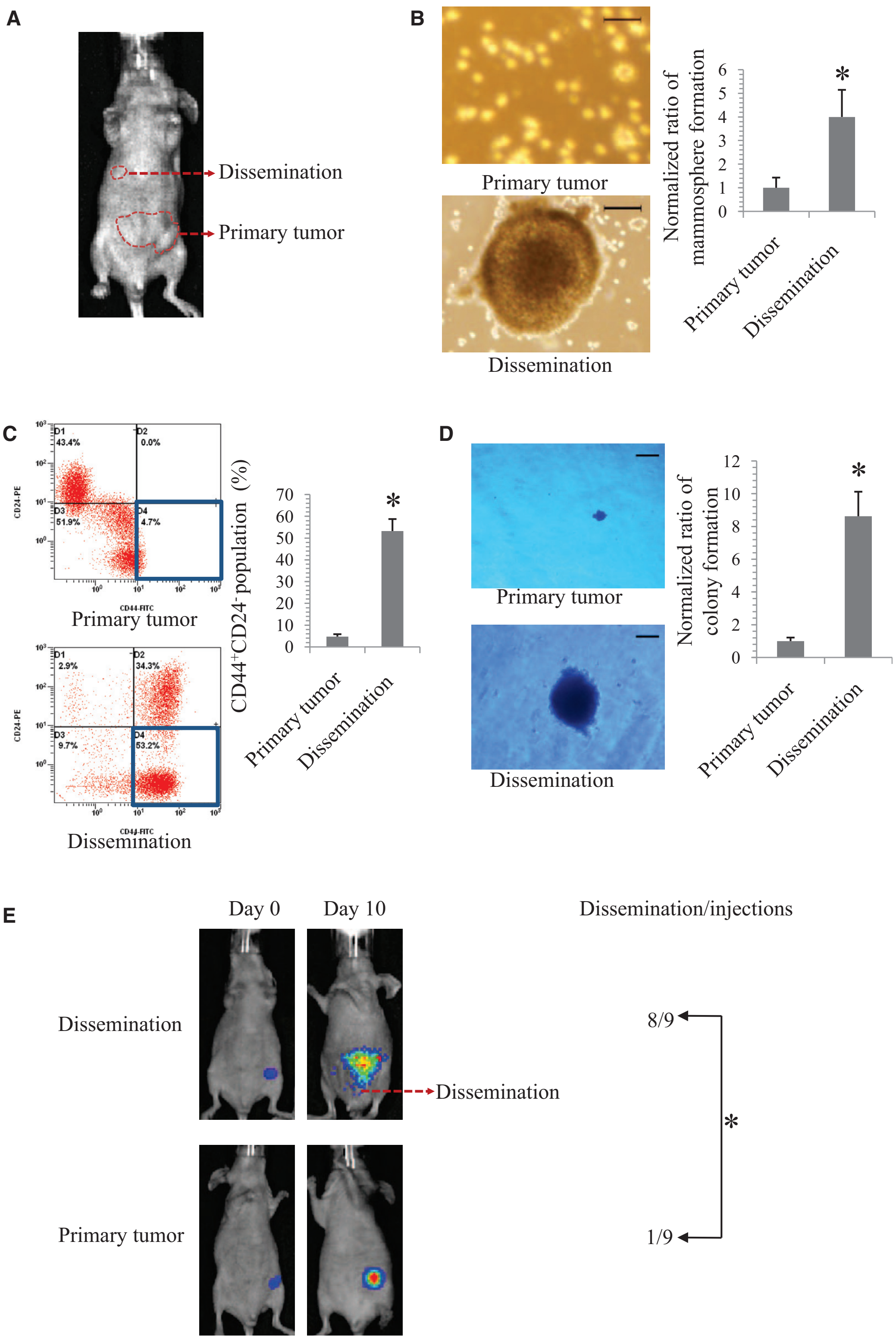

(legend on next page)

modality, nanoparticle delivery, has been highlighted as a promising solution for refractory cancer.[10] Nanoparticle delivery enhances therapeutic efficacy of cancer, whereas minimizing off-target toxicity. Previously, our group has integrated the VP16-GAL4-woodchuck hepatitis virus post-transcriptional regulatory element (WPRE)-integrated systemic amplifier (VISA), which has a significant antitumor effect on pancreatic tumors with almost no toxicity.[11] Subsequently, we found that VISA-claudin4-BikDD treatment dramatically reduces the $CD44^{+}CD24^{-}$ population of BC cells.[12] Later, we developed a versatile TV (human telomerase reverse transcriptase [hTERT] promoter-driven VISA [T-VISA]) amplifier delivery to target transgene expression in breast tumors, which has comparable or even stronger activity than that of the cytomegalovirus promoter in cancer cells.[13,14] More recently, we developed a TV delivery of microRNA (miR)-34a, which reduces proliferation of BCSCs effectively and safely.[7] Both hTERT expression and telomerase activity in healthy mammary epithelial cells (HMECs) were significantly inferior to either BC cells or BCSCs. Further, we found that the hTERT promoter can direct preferential transgene expression in BC cells and BCSCs, rather than HMECs.[7] Detailed analyses of molecular mechanisms indicate that telomeres can form G-quadruplex structures (G4) in adult stem cells. Moreover, structures of G4 are highly stable and are difficult to resolve during replication, which can cause replication fork stalling.[15] Therefore, TV delivery has the appropriate construction to express targeted molecules via an efficient and safe approach. In the present study, we explored this novel therapeutic avenue for feasible treatment of metastasis by using long-term-cultured BCSCs.

Circular RNAs (circRNAs) are a novel type of endogenous noncoding RNA characterized as stable, abundant, and conserved. The high degree of conservation of circRNAs suggests that this family plays an important role in the organism. A lot of studies have revealed that circRNAs participate in the development of progenitor cells. For instance, RNA-binding protein FUS affects the expression of circRNAs in murine embryonic stem cell-derived motor neurons.[16] Recent studies also revealed that circRNAs HECTD1 and ZNF91 regulate epidermal stem cell differentiation.[17] Expression profiles of circRNAs were significantly altered during osteogenic differentiation of periodontal ligament stem cells.[18] For example, circRNAs BIRC6 and CORO1C are functionally associated with the pluripotent state in undifferentiated human embryonic stem cells.[19] hsa_circ_0067531 alters the biological function of $CD90^{+}$, a marker for the hepatic CSCs, in hepatocellular carcinoma cells.[20] All of this evidence indicates that circRNA interference can mediate stem-like properties in cancer cells. However, whether circRNAs have the property to regulate metastatic CSCs remains to be explored.

With this in mind, we exploited a feasible biological rationale of the association between metastatic status and tumor-initiating properties in metastatic BCSCs. Further, we explored the most prominent circRNA in tumor tissue-derived or cell line-derived long-term-cultured BCSCs. Furthermore, we determined the therapeutic responses of TV delivery of the specific circRNA on metastatic BCSCs. Additionally, we provided mechanistic insight of this therapeutic strategy and the tolerability of this nonviral liposomal nanoparticle.

RESULTS

Metastatic BC Cells Show Stem-like Properties

Preliminarily, in order to determine the biological properties of metastatic BC cells, we generated a mouse model of the MCF-7 BC xenograft using the female non-obese diabetic/severe combined-immunodeficient (NOD/SCID) mouse (Figure 1A). Next, we distinguished the stem-like properties of the cancer cells derived from primary and metastatic tumors of the xenograft model. Metastatic tumors display to disseminate *in vivo*. The stem-like properties of primary tumors were compared with their corresponding disseminations in MCF-7-bearing athymic female NOD/SCID mice. Compared to those cells derived from corresponding primary tumors, cells derived from metastatic tumors displayed stronger stem-like properties, evidence by the increased mammosphere-forming capacity (Figure 1B), higher proportion of $CD44^{+}CD24^{-}$ (Figure 1C), and enhanced clonogenicity in soft agarose (Figure 1D).

Further, we explored whether metastatic BC cells are prone to develop dissemination. With the use of a mouse model of the xenograft, we found that mice bearing the BC cells derived from the metastatic MCF-7 tumor have higher risk of disseminated cancers than the mice-bearing cancer cells derived from the primary MCF-7 tumor, i.e., 8 of 9 for the former versus 1 of 9 for the latter (Figures 1E and S1). This result demonstrated that metastatic BC cells are more prone to disseminate *in vivo*. Taken together, we initially explored that metastatic BC cells are rich in stem-like properties and are more prone to disseminate.

BCSCs Mediate BC Metastasis

To determine whether disseminated BC cells directly originate from the corresponding primary cancer cells, immunohistochemistry

Figure 1. Identification of Stem-like Properties of Metastatic Breast Cancer Cells

(A) Image of primary tumor and dissemination in an MCF-7 tumor-bearing mouse was representative of 12 independent experiments. (B) Representative images (left panel) and statistical results (right panel) of the mammosphere-forming capacity of cancer cells derived from MCF-7 primary and metastatic tumors. Scale bars, 100 μm. Mammospheres larger than or equal to 50 μm in diameter were counted. Statistical analysis was performed using the Mann-Whitney U test. (C) Representative images (left panel) and statistical results (right panel) of a higher percentage of $CD44^{+}CD24^{-}$ subpopulation in cancer cells derived from an MCF-7 metastatic tumor compared to those derived from a primary tumor. Statistical analysis was performed using the paired t test. (D) Representative images (left panel) and statistical results (right panel) of colony formation in soft agar. Scale bars, 100 μm. Spheres of colony formation greater than equal to 50 μm in diameter were analyzed. Statistical analysis was performed using the Mann-Whitney U test. (E) Representative IVIS spectrum images (left panel) and statistical results (right panel) of dissemination in luciferase-labeled, 20th-passage MCF-7.SC- and primary breast cancer (BC) cell-bearing mice (n = 9 per group). Data are expressed as mean ± SD. Statistical analysis of (E) was performed using Fisher's exact test. All experiments were repeated more than five times unless indicated otherwise. *$p < 0.05$ was considered as statistically significant.

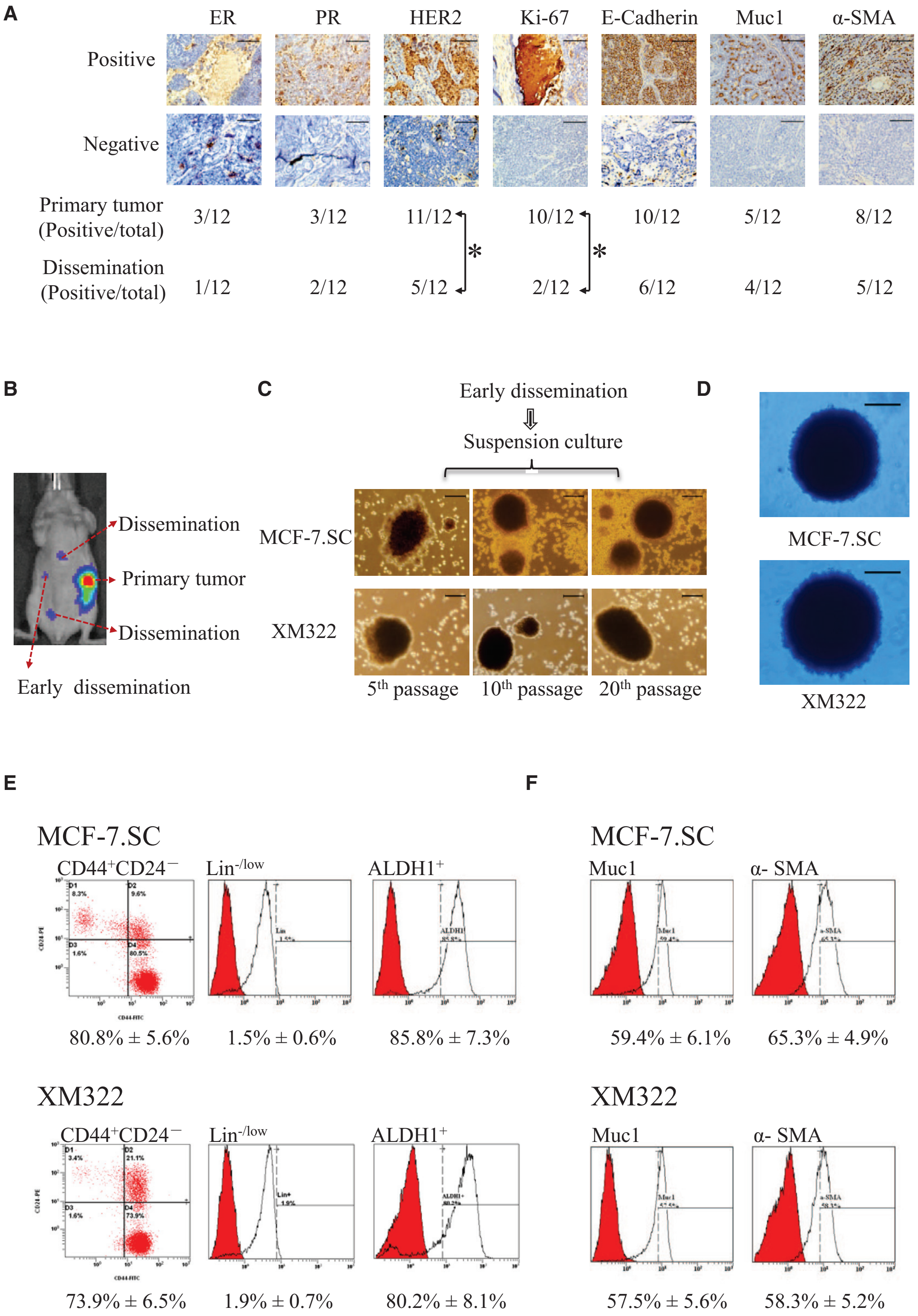

(legend on next page)

(IHC) for biomarker expression, including estrogen receptor (ER), progesterone receptor (PR), human epidermal growth factor (EGF) receptor 2 (HER2), Ki-67, E-cadherin, mucin 1 (Muc1), and α-smooth muscle actin (SMA), was applied to specimens of primary tumors and metastasized tumors in the MCF-7-bearing mice (Figure 2A). Protein expressions of the above-mentioned biomarkers in the metastatic tumors are different from their corresponding primary tumors (Figure 2A). Among them, positive rates of both HER2 and Ki-67 expressions are significantly different from those in the disseminated tumors. These results indicated that disseminated tumor cells did not originate from their primary cancer cells directly.

It is well known that CSCs maintain the capability of pluripotency. The early disseminated cancer cells potentially reflected the characteristics of metastatic tumor cells.[21] Therefore, we tried to investigate the tumor-initiating properties of early disseminated cancer cells in tumors of luciferase-labeled BCSC-bearing mice (Figure 2B). The mouse models of the BCSC xenograft were generated using the previous reported BCSCs, MCF-7.SC and XM322.[7,8] We found that early disseminated tumor cells derived from the MCF-7.SC- and XM322-bearing mice displayed stem-like abilities, evidenced by the properties of mammosphere formation (Figure 2C) and abilities of colony formation in soft agarose (Figure 2D). A high percentage of the $CD44^{+}$ $CD24^{-}$ subpopulations was also observed in early disseminated tumor cells derived from the MCF-7.SC- and XM322-bearing mice. These subpopulations of cells had no or low expression of lineage (Lin) but high expression of ALDH1 ($CD44^{+}CD24^{-}Lin^{-/low}$ $ALDH1^{+}$) (Figure 2E). Furthermore, early disseminated tumor cells showed the pluripotent ability, as high expression of Muc1 and α-SMA was observed in flow cytometry analysis after differentiation culture (Figure 1F). Altogether, we demonstrated that BCSCs, at least partially, mediated metastasis in BC.

circRNA RANBP2-like and GRIP Domain-Containing Protein 6 (circRGPD6) Is the Most Promising circRNA for Potential Therapy of BCSCs

circRNAs act as microRNA (miRNA) sponges, regulate gene expression by influencing the transcription, and have the potential abilities to inhibit tumor progression;[22] therefore, we further explored the potential intervention of circRNA to BCSCs. We tried to reveal the high expression miRNAs in malignant breast cells (BC and BCSCs), as well as with the miRNAs with a higher level in BCSCs, we performed further evaluation of the above miRNAs. With the use of a genome-wide miRNA array, we screened the miRNA profiles in immortal HMEC lines (184A1 and MCF-12A), BC cell lines (BC, MCF-7, MDA-MB-231, MDA-MB-468, and SK-br-3), and BCSCs (MCF-7.SC, MDA-MB-231.SC, XM322, and XM607). These results are available at ArrayExpress (accession number E-MTAB-5584; https://www.ebi.ac.uk/arrayexpress/experiments/E-MTAB-5584). As a result of miRNA profiling, miRNA upregulation in BC and BCSCs was revealed compared to HMEC. Compared with HMEC, the following 20 miRNAs are upregulated in both BC and BCSCs: miR-103a-3p, miR-107, miR-1234-5p, miR-125b-5p, miR-151a-5p, miR-15b-5p, miR-21-5p, miR-23b-3p, miR-24-3p, miR-26b-5p, miR-27b-3p, miR-29a-3p, miR-29b-3p, miR-365a-3p, miR-4443, miR-4459, miR-4530, miR-494-3p, miR-6087, and miR-6088 (Figure 3A). Next, quantitative reverse transcriptase-PCR (qRT-PCR) analysis was also performed to confirm the expressions of these miRNAs. Compared with HMEC, the expressions of miR-103a-3p, miR-107, miR-125b-5p, miR-15b-5p, miR-21-5p, miR-23b-3p, miR-24-3p, miR-26b-5p, miR-27b-3p, miR-29a-3p, and miR-29b-3p are at least 2 times upregulated in BC and BCSCs. Intriguingly, the expressions of these 11 miRNAs were also increased compared to BC (Figure 3B). We then used starBase, which is a database for exploring miRNA and circRNA interaction, to identify the circRNAs that can sponge the above-mentioned upregulated miRNAs (http://starbase.sysu.edu.cn/).[23] From these results, we found that circRGPD6 was the most promising circRNA to sponge the miRNAs that are highly upregulated in BCSCs and thereby could be used as a potential therapeutic target in BCSCs (Figure 3C; Table S1).

In order to confirm these results, we performed a qRT-PCR analysis to quantify the expression of circRGPD6 in clinical BC specimens. We randomly recruited 22 clinical cases with BC, including 6 cases with metastatic BC. We observed that circRGPD6 expression in primary tumors was significantly lower than that in adjacent healthy breast tissues (HBTs), whereas metastatic tumors had significantly decreased in circRGPD6 expression compared with adjacent HBTs and primary tumor (Figure 3D). Further, we extended the observation of circRGPD6 expression to cell lines. Consistently, compared with the two immortalized HMECs (184A1 and MCF-12A), circRGPD6 expressions in BC and BCSCs were significantly decreased (Figure 3E). Additionally, circRGPD6 expressions in BCSCs were significantly lower than that in BC (Figure 3E). Over the four BCSCs, XM322 cells showed the lowest expression of circRGPD6 followed by MCF-7.SC. Thus, we selected MCF-7.SC cells and XM322 cells as the representative BCSCs in most of the following experiments, unless indicated otherwise.

Figure 2. BC Stem Cells (BCSCs) Mediate BC Metastasis

(A) Representative microscope images of IHC for ER, PR, HER2, Ki-67, E-cadherin, Muc1, and α-SMA (top panel) and the corresponding results (bottom panel) in the primary and metastatic tumors of MCF-7-bearing mice. $^{*}p < 0.05$ was considered as statistically significant using the Fisher's exact test (n = 12). (B) IVIS spectrum images of early disseminated cancer cells in the tumor of luciferase-labeled MCF-7.SC- or XM322-bearing mice were representative of five independent experiments. (C) Representative microscope images of mammospheres formed from the early disseminated cancer cell derived from MCF-7.SC- and XM322-bearing mice. (D) Representative images of colony formation in soft agarose for early disseminated tumor cells derived from MCF-7.SC (top panel)- and XM322 (bottom panel)-bearing mice. (E) Flow cytometry analysis of $CD44^{+}CD24^{-}Lin^{-/low}ALDH1^{+}$ expressions in the early disseminated cancer cells derived from MCF-7.SC- and XM322-bearing mice. Peaks labeled in red represent isotype control. (F) Flow cytometry analysis of Muc1 and α-SMA expressions assessing pluripotent capabilities of the early disseminated cells derived from MCF-7.SC- and XM322-bearing mice. Peaks labeled in red represent isotype control. All experiments were repeated at least in triplicate. Scale bars, 100 μm.

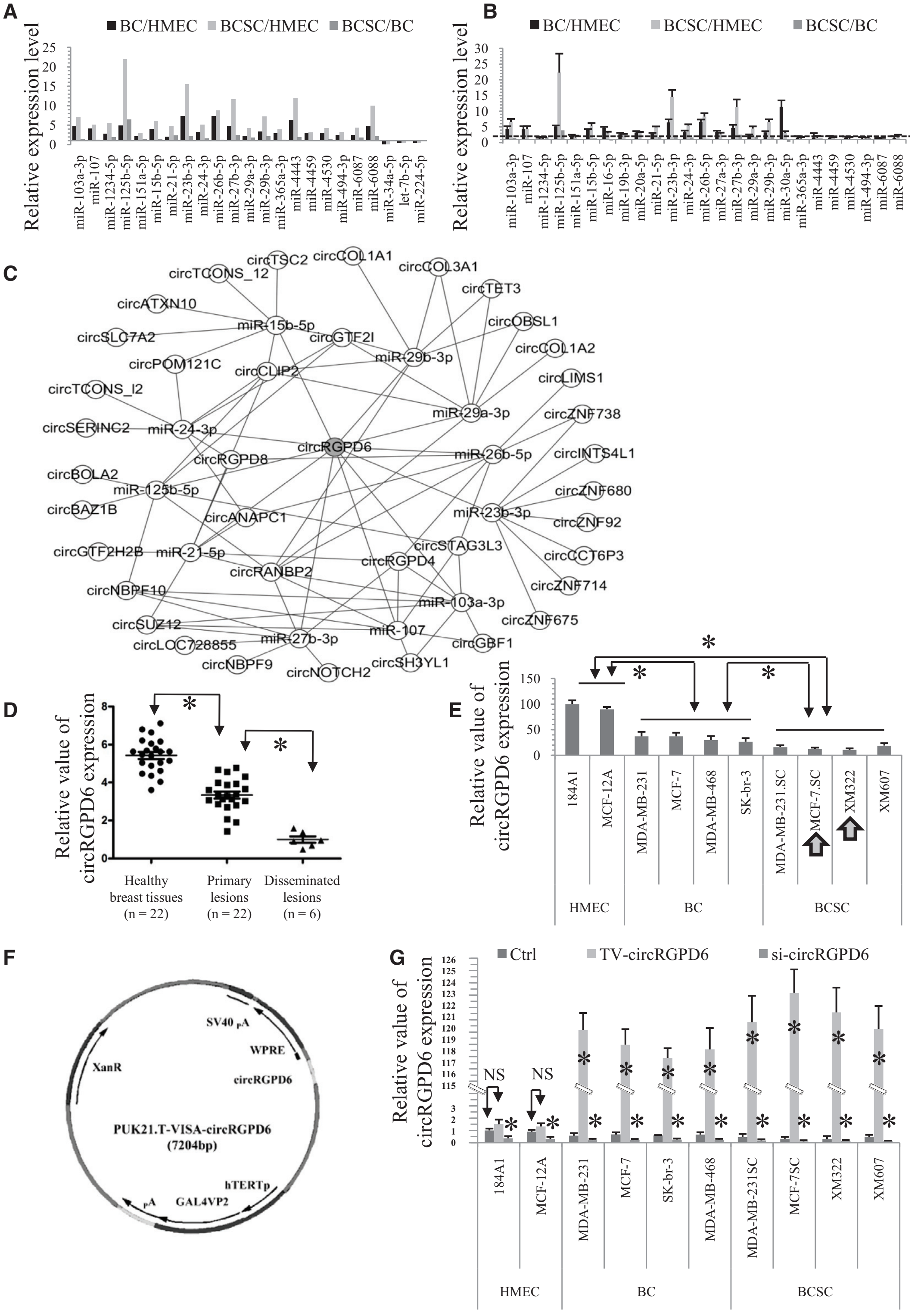

Figure 3. circRGPD6 Is the Most Promising Circular RNA (circRNA) for BCSC Therapy

(A) Genome-wide microRNA (miRNA) expression profiling in BC cells and BCSCs. Date was normalized to immortalized healthy mammary epithelial cells (HMEC) and relative to BC. (B) qRT-PCR of microRNA expressions in BC, BCSCs, and HMECs. (C) starBase analysis of miRNA-circRNA interactions predicting that circRNAs sponge the

(legend continued on next page)

To investigate the potential regulation of circRGPD6 on tumor-initiating properties of BCSCs, we constructed the regulators of circRGPD6. Based on our previous studies,[7,11–13] a versatile hTERT-based BC-specific promoter VISA composite to overexpress circRGPD6 (TV-circRGPD6) was developed (Figure 3F). RT-PCR confirmed that TV-circRGPD6 significantly enhanced the expression of circRGPD6 in both BC and BCSC, rather than immortalized HMEC (Figures S2A–S2E). Furthermore, the CircInteractome network was performed to design 2 silence sequences of circRGPD6 (si-circRGPD6-1 and si-circRGPD6-2) (https://circinteractome.nia.nih.gov/).[24] We knocked down circRGPD6 expression in HMEC, BC, and BCSCs by using circRGPD6 small interfering RNA (siRNA). The efficiency of circRGPD6 silencing was confirmed by qRT-PCR (Figures S2F–S2J). Similarly, circRGPD6 siRNA significantly decreased the expression of circRGPD6 in both BC and BCSCs, rather than immortalized HMEC (Figures S2F–S2J). To rule out the possibility that circRGPD6 siRNA might exert effects on the mRNA level of RGPD6 (linear RGPD6), we analyzed the RGPD6 mRNA level and found no significant changes (Figures S2F–S2J). Therefore, we chose si-circRGPD6-1 to perform further experiments based on its higher knockdown efficiency.

Following, qRT-PCR analyses found that circRGPD6 expressions were rarely altered in both HMEC cells (184A1 and MCF-12A) under the condition of upregulation (TV-circRGPD6); however, circRGPD6 expressions were significantly inhibited by si-circRGPD6 (Figure 3G). However, in comparison with the control (Ctrl), the relative value of circRGPD6 expression in TV-circRGPD6-transfected BC increased approximately 250-fold, whereas the circRGPD6 relative value in TV-circRGPD6-transducted BCSCs increased approximately 300-fold (Figure 3G). Conversely, si-circRGPD6 significantly increased circRGPD6 expression in both BC and BCSCs. These results can be explained by the findings of Cao et al.[25] and our previous studies for HMEC.[7] Although mRNA and protein expression of hTERT could be upregulated in expressing exogenous hTERT-amplified HMEC, human telomerase RNA (hTR) limits telomerase activity and telomere maintenance in the context of hTERT amplification. Therefore, TV-circRGPD6 drives the expression of circRGPD6 selectively in BCSCs and BC but does not drive its expression in HMEC. We found that MCF-7.SC cells showed the highest expression of circRGPD6 under treatment with TV-circRGPD6, and XM322 cells showed the second-highest expression of circRGPD6 (Figure 3G). In sum, TV-circRGPD6 induced high throughput of circRGPD6 expressions in both BC and BCSCs.

Characteristics of circRGPD6 in BCSCs

Preliminarily, we investigated the stability of circRGPD6 in both MCF-7.SC and XM322. Total RNAs of MCF-7.SC and XM322 cells were isolated at the indicated time points under treatment with actinomycin D, an inhibitor of transcription. Then, qRT-PCR was performed to measure mRNA expression of circRGPD6 and linear RGPD6. The results showed that the half-life of circRGPD6 exceeded 24 h, whereas that of linear RGPD6 was approximately 3.5 h in both MCF-7.SC cells and XM322 (Figure S3A). Next, in order to rule out the possibility that the head-to-tail splicing products may also derive from genomic rearrangements and *trans*-splicing, we performed a qRT-PCR assay with specially designed divergent and convergent primers and discovered that circRGPD6, but not linear RGPD6 or glyceraldehyde 3-phosphate dehydrogenase (GAPDH), could resist digestion by RNase R (Figure S3B). Moreover, we confirmed the expression of back-spliced or canonical forms of RGPD6, with or without RNase R supplementation in the cDNA and genomic DNA (gDNA) of BCSCs by PCR and visualized by an agarose gel electrophoresis assay (Figure S3C). Subsequently, Northern blots were performed to validate circRGPD6 expression following transfection with TV-circRGPD6 in BCSCs. Results indicated that the nonviral TV-circRGPD6 nanoparticle successfully overexpressed circRGPD6 (Figure S3D). To summarize, circRGPD6 was confirmed to be a circRNA; its stable and loop structure facility its role in BCSC intervention.

TV-circRGPD6 Nanoparticle Inhibits Tumor-Initiating Properties of BCSCs *In Vitro*

CSC-associated tumor-initiating properties are highly associated with tumor progression.[26] Here, we explored the influence of circRGPD6 on stem-like properties in 20th-passage BCSCs. Interestingly, we found that TV-circRGPD6 reduced the proportion of $CD44^{+}CD24^{-}$ in both MCF-7.SC and XM322, whereas si-circRGPD6 increased the subpopulation of these cells using flow cytometry analysis (Figures 4A and S4A). For the purpose of evaluating the influence of circRGPD6 on CD44 expression in BCSCs, we constructed a TV-circRGPD6-GFP nanoparticle and performed the clonal pair-cell assays in BCSCs treated with the nanoparticle. Encouragingly, clonal pair-cell assays demonstrated that TV-circRGPD6 significantly suppressed CD44 expression in both MCF-7.SC and XM322 (Figure 4B). Next, we investigated whether decreased CD44 expression leads to cell death of BCSCs after TV-circRGPD6 treatment. Clonal pair-cell assays showed that decreased CD44 expression induced by TV-circRGPD6 was associated with a higher expression of phospho-H2AX (p-H2AX), a marker of DNA damage, in both MCF-7.SC and XM322 (Figure 4C). We also noticed that increased expression of p-H2AX was associated with the damage of nuclei, evidence by decreased 4′,6-diamidino-2-phenylindole (DAPI)-positive staining in BCSCs (Figure 4C). Further, we exploited that TV-circRGPD6 transfection also enhanced the pluripotency capabilities in BCSCs, evidence by

above-regulated miRNAs. circRGPD6 was identified as the most pronounced circRNA for sponging the regulated miRNAs in (A) and (B). (D) qRT-PCR analysis of circRGPD6 expression in healthy breast tissues, primary tumors, and disseminated lesions. (E) qRT-PCR analysis of circRGPD6 expressions in HMEC (184A1 and MCF-12A), BC (MCF-7, MDA-MB-231, MDA-MB-468, and SK-br-3), and BCSCs (MCF-7.SC, MDA-MB-231.SC, XM322, and XM607). (F) Schematic structure of TV-circRGPD6. (G) qRT-PCR analysis of circRGPD6 expressions in HMEC (184A1 and MCF-12A), BC (MCF-7, MDA-MB-231, MDA-MB-468, and SK-br-3), and BCSC (MCF-7.SC, MDA-MB-231.SC, XM322, and XM607), with or without TV-circRGPD6 and si-circRGPD6 transfection. Each experiment was repeated more than three times. $^{*}p < 0.05$; NS, not significant. Statistical analysis was performed using the paired t test.

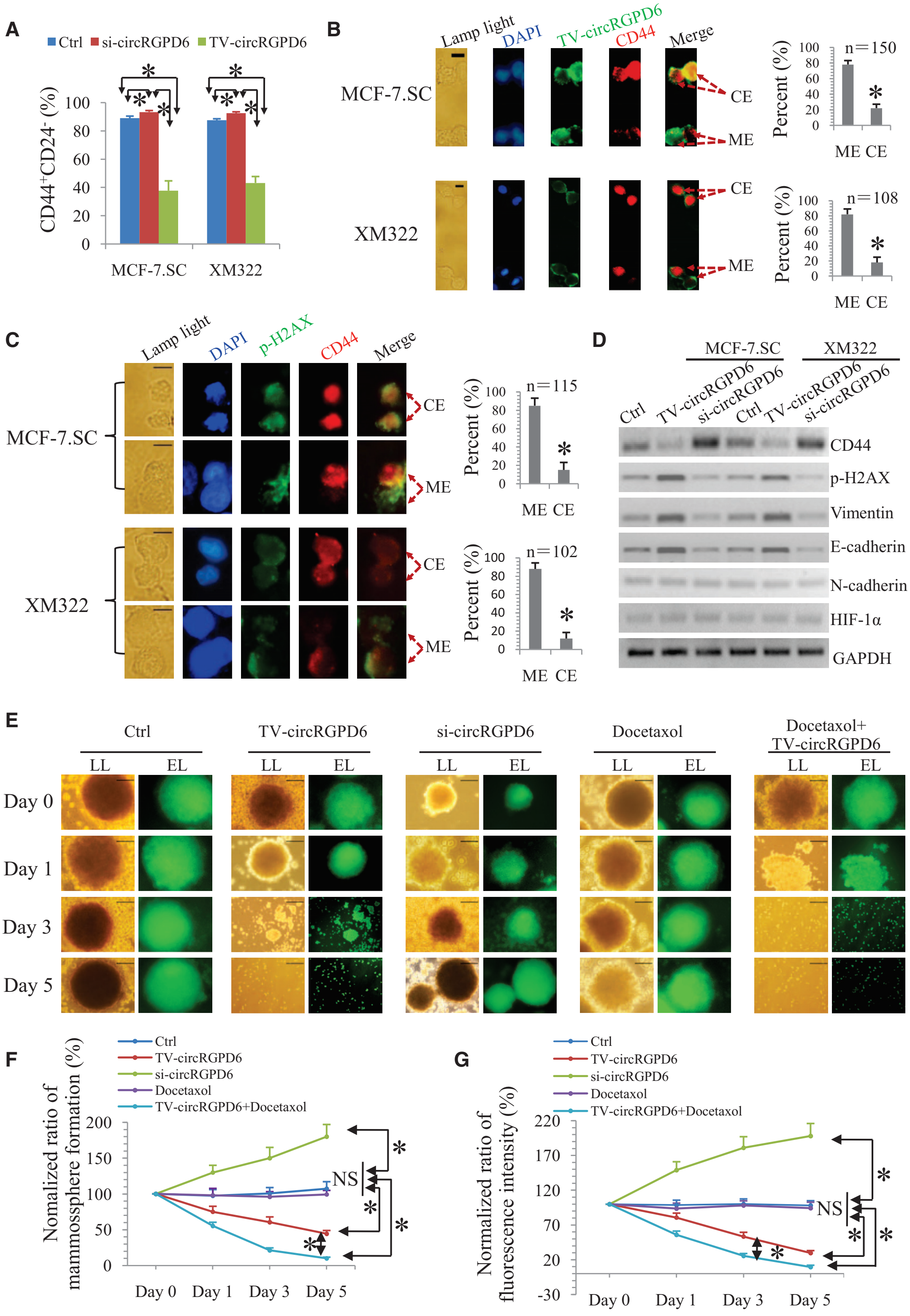

(legend on next page)

increased expression of differentiation makers, e.g., Muc1 and α-SMA (Figure S4B). Since expressions of CD44, vimentin, E-cadherin, N-cadherin, and hypoxia-inducible factor 1-alpha (HIF-1α) are proposed to be involved in maintenance of tumor-initiating properties and pluripotency in CSCs,[9] we investigated whether circRGPD6 changes their expressions of these mentioned molecules in 20th BCSCs. Western blot analyses showed that TV-circRGPD6 inhibited CD44 expression and elevated the expressions of p-H2AX, vimentin, and E-cadherin in both MCF-7.SC and XM322, whereas si-circRGPD6 increased CD44 expression but decreased expressions of p-H2AX, vimentin, and E-cadherin. However, circRGPD6 did not alter the expressions of N-cadherin and HIF-1α in BCSCs (Figure 4D). In sum, these results demonstrated that low expression of circRGPD6 enhanced the maintenance of stem-like characteristics, and TV-circRGPD6 significantly suppressed the tumor-initiating properties of BCSCs.

Owing to TV-circRGPD6 holding the potential abilities to promote BCSCs to convert into nonstem-like cells, we further examined whether TV-circRGPD6 synergizes with taxanes to eradicate BCSCs. Taxanes are a class of chemotherapy compounds, e.g., docetaxel, which are widely used as the standard therapy for invasive BC. In this study, we determined the therapeutic effect of a combination of TV-circRGPD6 and docetaxel on XM322. To evaluate the combined effect, we generated GFP-labeled BCSCs. We observed that TV-circRGPD6 alone inhibited mammosphere-formation capacity and fluorescence intensity of GFP-labeled BCSCs (Figures 4E and 4F). To evaluate the synergistic effect of docetaxel on TV-circRGPD6, docetaxel was added at a concentration of 2 nM.[27] Although the results showed that docetaxel alone did not influence the mammosphere-formation capacity and fluorescence intensity of BCSCs, a combination of docetaxel and circRGPD6 significantly decreased mammosphere-formation capacity and fluorescence intensity of BCSCs more than TV-circRGPD6-alone treatment did (Figures 4E and 4G). Similar results were found in 3-(4,5-dimethylthiazol-2-yl)-2,5-diphenyltetrazolium bromide (MTT) assays. Docetaxel alone did not affect cell viability of XM322, but a combination use of docetaxel and TV-circRGPD6 significantly inhibited cell viability of XM322 more that TV-circRGPD6 alone did. Conversely, si-circRGPD6 significantly increased the viability of XM322 (Figure S4C). In summary, TV-circRGPD6 synergized with docetaxel in eradication of BCSCs *in vitro*.

TV-circRGPD6 Suppresses Stem-like Properties of Metastatic BC Tumors *In Vivo* and Synergizes with Docetaxel for Inhibition of Proliferation and Metastasis of BC

We next determined the protective effect of TV-circRGPD6 against the stem-like properties of metastatic BC tumors *in vivo*. The mouse model of the BCSC xenograft was generated using XM322 with expression of firefly luciferase. Initially, we found that TV-circRGPD6 inhibited the growth of tumors in the XM322-bearing mice in a dose-dependent manner (Figure 5A). Based on the principle of efficacious antitumor activity with lower potential toxicity, 10 μg every other day (qod) of TV-circRGPD6 was chosen as the optimum dose to achieve the antitumor efficacy but avoid the potential toxicity in XM322-bearing mouse model (Figure 5A). Meanwhile, 10 mg/kg qod of docetaxel via tail-vein intravenous injection was administered to the mice every 2 days for 20 days.[28] With the goal of achieving an orthotopic model of BC metastasis, mice with metastatic tumors and their corresponding primary tumors showing luminescent photon signals at $\sim 500 \times 10^6$ photons/s were included for the following 20-day investigation of TV-circRGPD6, si-circRGPD6, docetaxel, and docetaxel plus TV-circRGPD6 (Figures 5B and S5). We observed that si-circRGPD6 significantly promoted metastasis procession in tumors of XM322-bearing mice. Conversely, TV-circRGPD6 inhibited the metastasis procession of the tumors. Moreover, TV-circRGPD6 synergizes with docetaxel against proliferation and metastasis of BC cells in XM322-bearing mice (Figures 5B and S5). Stem-like biological properties of metastatic BC tumors in XM322-bearing mice after different interventions were also characterized. Fine-needle aspiration biopsy of tumors was done at baseline (day 0) and 20 days (day 20) after the commencement of interventions for assessment of the $CD44^+CD24^-$ subpopulation by flow cytometry. We found the early disseminated tumor cells had a very high percentage of $CD44^+CD24^-$ subpopulation on both day 0 and day 20 (Figure 5C). We also found that the proportion of $CD44^+CD24^-$ cells in the early disseminated tumor was higher than that in the dissemination lesion (Figure 5C). In particular, after 20 days of intervention, TV-circRGPD6 plus docetaxel significantly suppressed the $CD44^+CD24^-$ CSC population in primary, disseminated, and early disseminated tumors of XM322-bearing mice more than TV-circRGPD6 alone did, although docetaxel alone promoted the proportion of $CD44^+CD24^-$ in primary and disseminated tumors (Figure 5C). Importantly, luminescent imaging reflected the same result—that combined usage of TV-circRGPD6 and docetaxel presented displayed better inhibitory

Figure 4. TV-circRGPD6 Inhibits Tumor-Initiating Properties of BCSCs *In Vitro*

(A) Flow cytometry analysis of $CD44^+CD24^-$ expressions in MCF-7.SC and XM322 after transfection of either si-circRGPD6 or TV-circRGPD6. (B) Representative microscope images of coimmunofluorescence (left panel) as well as statistical results (right panel) of TV-circRGPD6-GFP and CD44-phycoerythrin (PE) are either mutually exclusive (ME) or coexpressed (CE) in at least one of the daughter cells during BCSC divisions. Scale bars, 10 μm. (C) Representative microscope images of coimmunofluorescence (left panel) as well as statistical results (right panel) of p-H2AX and CD44 expression in daughter cells of BCSCs during division after transfection of TV-circRGPD6 in clonal pair-cell assays. Scale bars, 10 μm. (D) Western blots for CD44, p-H2AX, vimentin, E-cadherin, N-cadherin, HIF-1α, and GAPDH expression in MCF-7.SC and XM322, with or without transfection of TV-circRGPD6 and si-circRGPD6. (E) TV-circRGPD6 synergizes with docetaxel to eradicate XM322. Representative bright field or fluorescence images of XM322 in mammosphere-formation assay. XM322, which is GFP labeled, was treated with TV-circRGPD6, si-circRGPD6, docetaxel, and TV-circRGPD6 plus docetaxel, respectively. Bright field (lamp light [LL]; left panel) or laser with excitation wavelength (EL; right panel) was used to detect the depression effects. Scale bars, 100 μm. (F and G) Quantification of (F) mammosphere formation and (G) fluorescence expressions of XM322 after treatments of Ctrl, TV-circRGPD6, si-circRGPD6, docetaxel, and docetaxel combined with TV-circRGPD6. Mammospheres larger than or equal to 50 μm in diameter were counted. Statistical analyses were performed using the paired t test. Each experiment was repeated at least three times. *$p < 0.05$; NS, not significant.

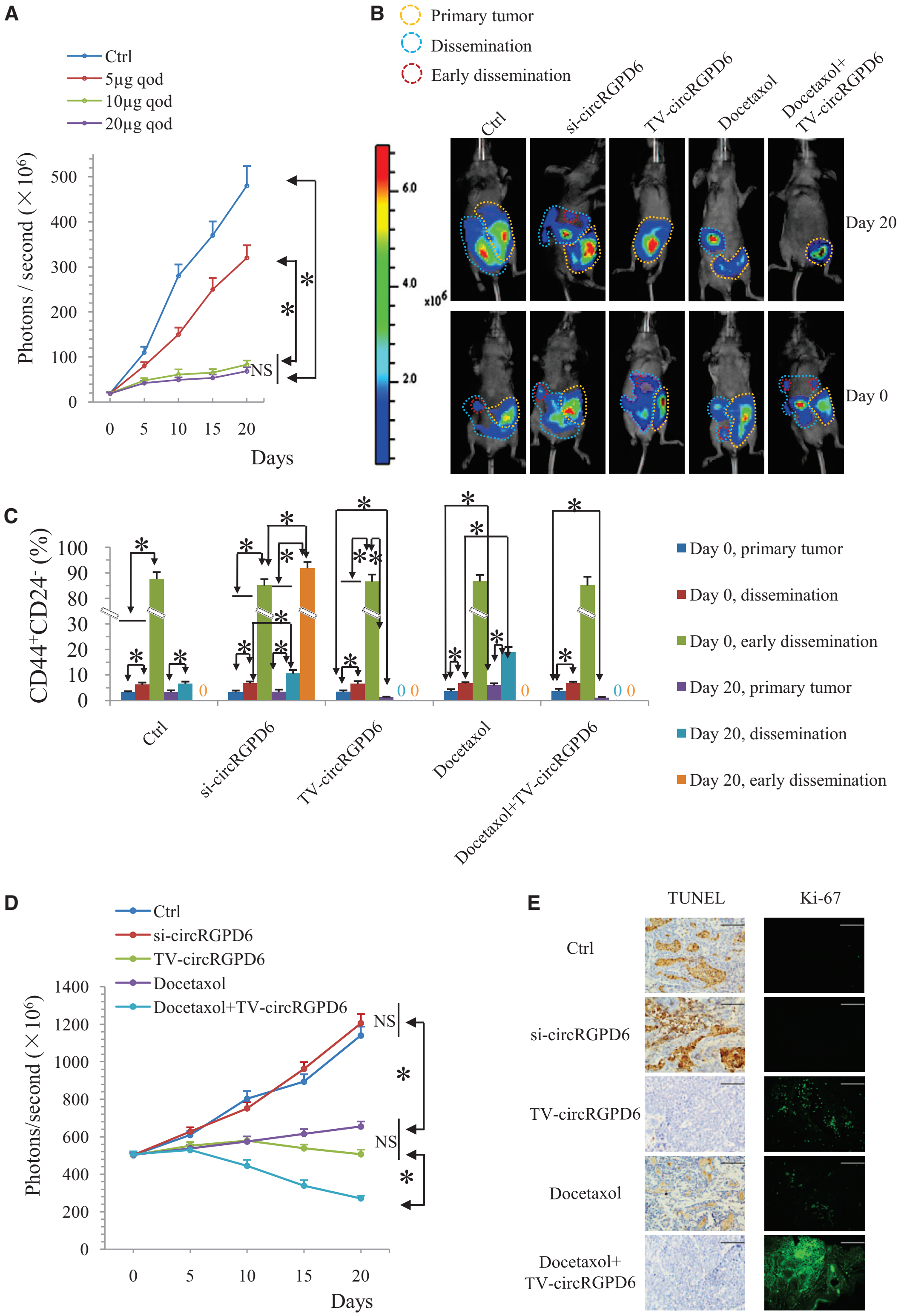

(legend on next page)

efficacy than just TV-circRGPD6 alone or docetaxel alone (Figure 5D). Furthermore, we determined the cell death using the TUNEL (terminal deoxynucleotidyl transferase-mediated deoxyuridine triphosphate [dUTP] nick end labeling) assay and cell proliferation using Ki-67 as a marker in the metastatic tumor of XM322-bearing mice after different interventions. Consistently, a decrease in TUNEL staining and increase in Ki-67 expression were observed in tumors of XM322-bearing mice treated with si-circRGPD6, whereas an increase in TUNEL staining and reduction in Ki-67 expression were seen in the group treated with TV-circRGPD6. Meanwhile, XM322-bearing mice treated with TV-circRGPD6 plus docetaxel showed the highest level of TUNEL staining and the lowest expression of Ki-67 in a metastatic tumor (Figure 5E). Taken together, these results suggested that TV-circRGPD6 inhibits stem-like properties of metastatic BC *in vivo*, and this effect synergizes with docetaxel against BC metastasis.

A safety concern of TV-circRGPD6 has also been considered. To determine whether TV-circRGPD6 takes effect on HMECs, we inoculated immortal HMEC cell 184A1 into the mammary fat pads of female nude mice for developing the orthotopic BC model. When tumors were established, TV-circRGPD6 or docetaxel was administrated to the mice for 20 days. Here, we found that neither TV-circRGPD6 nor docetaxel significantly plays an inhibitory effect on proliferation of 184A1-bearing tumors *in vivo* (Figures S6A and S6B). Further, we explored the potential toxicity of TV-circRGPD6 on BCSC-bearing mice by using mouse models of the XM322 xenograft. After up to 20 days treatments of Ctrl, si-circRGPD6, or TV-circRGPD6, we found no significant difference in the body weight of all XM322-bearing mice (Figure S6C). After treated with Ctrl, si-circRGPD6, or TV-circRGPD6, liver function of XM322-bearing mice was not changed, as indicated by the comparable serum alanine aminotransferase (ALT) (Figure S6D, top panel) and aspartate aminotransferase (AST) (Figure S6D, bottom panel). Similar concentrations of blood urea nitrogen (Bun) (Figure S6E, top panel) and serum creatinine (Cr) (Figure S6E, bottom panel) suggested that the renal function of XM322-bearing mice was not changed after treatment of Ctrl, si-circRGPD6, or TV-circRGPD6. Recently, the potential immunotoxicity of nanomaterial has received substantial concern.[29,30] Proinflammatory cytokines' secretion has been widely used to test the immunotoxicity of the nanomaterial. Here, we determined the serum proinflammatory cytokines, including tumor necrosis factor alpha (TNF-α), interleukin (IL)-6, and interferon (IFN)-γ, to assess the potential immunotoxicity of TV-circRGPD6 treatment *in vivo*. Both Ctrl-treated (liposome) and si-circRGPD6-treated XM322-bearing mice had a similar concentration of serum TNF-α, IL-6, and IFN-γ (Figures S6F–S6H). From day 0 to day 10, concentrations of serum TNF-α, IL-6, and IFN-γ were significantly increased in TV-circRGPD6-treated XM322-bearing mice by 5%~10% compared to Ctrl and si-circRGPD6-treatments (Figures S6F–S6H). After injection of empty vector (liposome 100 μL) for 10 days in mice, TNF-α was increased by ~5.5-fold relative to day 0 (Figure S6F; $p < 0.05$). The level of IL-6 was increased by ~3.8-fold relative to day 0 (Figure S6G; $p < 0.05$). Similarly, the secretion of IFN-γ was increased by ~5.9-fold as compared with day 0 (Figure S6H; $p < 0.05$). Therefore, compared to an increase of serum proinflammatory cytokines driven by 10-day treatment of liposome (3.8- to 5.9-fold), an increase of serum proinflammatory cytokines driven by TV-circRGPD6 treatment was moderate.

TV-circRGPD6 Serves as a miRNA Sponge for miR-26b

We further exploited the underlying mechanisms of TV-circRGPD6 eradicating BCSCs. Subsequently, we explored whether TV-circRGPD6 sponges miRNAs and which miRNAs are its target. An miRNA expression profile was performed in MCF-7.SC and XM322 after transfection of TV-circRGPD6 and si-circRGPD6 (http://starbase.sysu.edu.cn/) (Table S2).[23] We found that 12 miRNAs were significantly upregulated in both MCF-7.SC and XM322 (Figure 6A). These results are available at ArrayExpress (accession number E-MTAB-7556; https://www.ebi.ac.uk/arrayexpress/experiments/E-MTAB-7556). We then used a qRT-PCR assay to analyze the expression of these 12 upregulated miRNAs, namely miR-103-3p, miR-24-3p, miR-107, miR-27a-3p, miR-125b-5p, miR-27b-3p, miR-15b-5p, miR-148b-5p, miR-26b-5p, miR-23b-3p, miR-29b-3p, and miR-29a-3p, in the sponge complex from the circRGPD6 pulldown experiments in MCF-7.SC and XM322 cells. In this case, we observed the enrichment of circRGPD6 and miR-26b-5p in both BCSCs (Figure 6B), whereas other miRNAs did not show such close interactions with circRGPD6. To further verify the absorption of miR-26b-5p into circRGPD6, we used a specific biotin-labeled miR-26b-5p probe to capture circRGPD6 (Figure S7A). According to miRNA response element (MRE) analysis of starBase,[23] circBase,[31] and CircInteractome,[24] the top miRNA regulated by circRGPD6 was miR-26b-5p, in accordance with the positions of putative binding sites in the circRGPD6 sequence. The potential binding sites and mutated sites of the circRGPD6 sequence were presented in Figure 6C. Apart from the pulldown assay, we performed a dual-luciferase reporter assay to confirm the direct interaction between circRGPD6 and miR-26b-5p. HEK293T cells were cotransfected with miR-26b

Figure 5. TV-circRGPD6 Suppresses Stem-like Biological Properties of Metastatic BC Tumors *In Vivo*

(A) Quantified luminescent photon signal of tumors in the XM322-bearing mice treated with different doses of TV-circRGPD6 up to 20 days. TV-circRGPD6 inhibited the growth of luciferase-labeled XM322-bearing tumors in a dose-dependent manner. 10 μg qod is the optimum dose. (B) Luminescent images of tumors in XM322-bearing mice with interventions of TV-circRGPD6, si-circRGPD6, docetaxel, and docetaxel plus TV-circRGPD6 up to 20 days were representative for three independent experiments. (C) Flow cytometry analysis of the $CD44^{+}CD24^{-}$ cancer stem cell population in primary and metastatic tumors of XM322-bearing mice with interventions of TV-circRGPD6, si-circRGPD6, docetaxel, and docetaxel plus TV-circRGPD6 up to 20 days. (D) Quantified luminescent photon signal of tumors in XM322-bearing mice with interventions of TV-circRGPD6, si-circRGPD6, docetaxel, and docetaxel plus TV-circRGPD6 up to 20 days. (E) TUNEL assay and immunofluorescence for Ki-67 in metastatic tumors of XM322-bearing mice after treatment of Ctrl, si-circRGPD6, TV-circRGPD6, docetaxel, and docetaxel plus TV-circRGPD6. Scale bars, 100 μm. Each experiment was repeated at least three times. $^{*}p < 0.05$; NS, not significant. Statistical analyses were performed using multifactor analysis of variance (univariate).

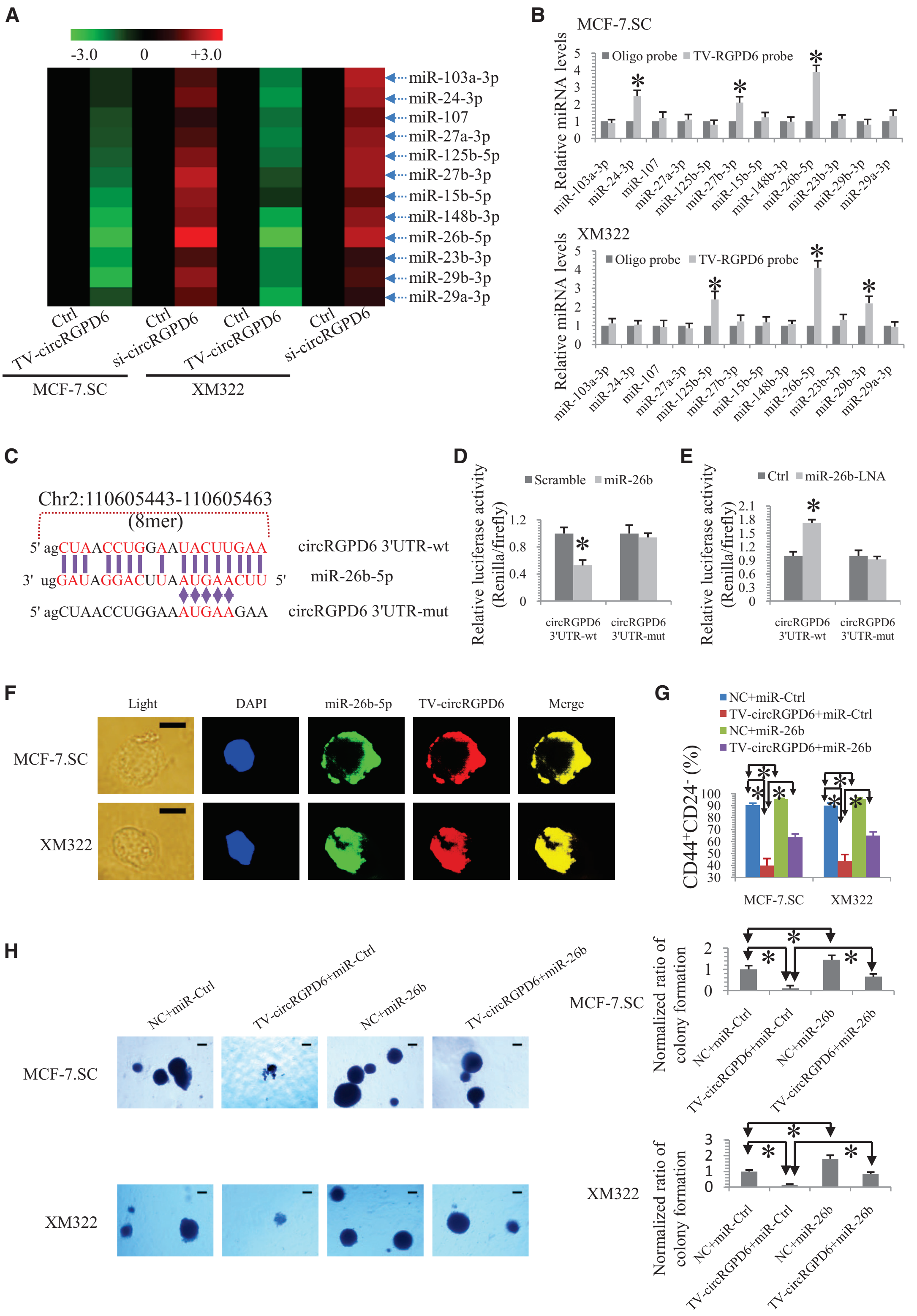

(legend on next page)

mimic and luciferase reporters. Luminescence intensity was reduced by approximately 55% in response to miR-26b mimics (Figure 6D). Moreover, HEK293T cells cotransfected with miRNA-26b LNA (locked nucleic acid), and luciferase reporters were performed to confirm the findings. Consistently, luciferase intensity was increased by approximately 70% in the miR-26b LNA-treated group (Figure 6E). In addition, qRT-PCR analysis revealed that miR-26b significantly reduced circRGPD6 expression (Figure S7B). Fluorescence *in situ* hybridization (FISH) analysis further showed miR-26b-5p was colocalized with TV-circRGPD6 in MCF-7.SC and XM322 (Figure 6F), which further suggested an interaction between TV-circRGPD6 and miR-26b-5p in BCSCs.

Furthermore, we determined whether miR-26b influences the effect of TV-circRGPD6 on stem-like properties of BCSCs. We found that cotransfection of miR-26b significantly reversed the decrease of the CD44$^+$CD24$^-$ proportion induced by TV-circRGPD6 in both MCF-7.SC and XM322 (Figure 6G). Similarly, the suppression effect of TV-circRGPD6 on colony formation was significantly aborted by miR-26b in both MCF-7.SC and XM322 (Figures 6H). In a word, TV-circRGPD6 serves as a miRNA sponge for miR-26b in BCSCs.

YAF2 (Yes-Associated Protein 2) Is a Direct Target of miR-26b and Upregulated by TV-circRGPD6

As current literature has highlighted the role of miRNAs in gene regulation in different tumors, we explored the potential downstream target of TV-circRGPD6/miR-26b. First, both MCF-7.SC and XM322 were treated with Ctrl, TV-circRGPD6, or si-circRGPD6. Genes that up- or downregulated more than two-fold ($p < 0.05$) were then included into gene lists of interest (Figure 7A; Table S3) and are available at ArrayExpress (accession number E-MTAB-7557; https://www.ebi.ac.uk/arrayexpress/experiments/E-MTAB-7557). The potential target genes were analyzed by using four algorithms: TargetScan,[32] miRDB,[33] TargetMiner,[34] and miRWalk,[35] to identify the putative cotarget genes of miR-26b. Interestingly, YAF2 was identified as the potential target of circRGPD6 and also as a direct target of miR-26b (Figure 7A). To confirm these results, we constructed a luciferase reporter vector with the full-length YAF2 3′ UTR containing target sites for miR-26b downstream of the luciferase gene (pGL3-YAF2 3′ UTR-wild type [WT]) and a mutant version of pGL3-YAF2-3′ UTR within the seed region (pGL3-YAF2 3′ UTR-mut) (Figure 7B). Encouragingly, miR-26b significantly reduced luciferase expressions of pGL3-YAF2-3′ UTR rather than pGL3-YAF2-3′ UTR-mut (Figure 7C) in HEK293T. In contrast, a significant increase in luciferase activity was observed when pGL3-YAF2-3′ UTR-WT was cotransfected with miR-26b inhibitors (miR-26b-LNA) but not with the pGL3-YAF2-3′ UTR-mut group (Figure 7D). qRT-PCR and western blot analyses were performed to confirm the luciferase assay results. We revealed that miR-26b significantly changed the mRNA expression of YAF2 in both MCF-7.SC and XM322 (Figure 7E). We also found that miR-26b and si-circRGPD6 significantly reduced YAF2 protein expression in both MCF-7.SC and XM322 cells, whereas miR-26b-LNA and TV-circRGPD6 enhanced protein expression of YAF2 (Figure 7F).

To evaluate the effect of the circRGPD6/miR-26b/YAF2 axis on stem-like properties of BCSCs, we further performed mammosphere-formation assay on BCSCs after treatments of Ctrl, TV-circRGPD6, miR-26b, miR-26b plus TV-circRGPD6, miR-26b plus YAF2 3′ UTR, and miR-26b plus YAF2 3′ UTR-mut-both. We found that the mammosphere-formation capacity of MCF-7.SC was significantly increased by TV-circRGPD6 but significantly increased by miR-26b (Figure 7G). Moreover, miR-26b significantly abated the inhibitory effect of TV-circRGPD6 in MCF-7.SC (Figure 7G). Interestingly, the promoting effect of the mammosphere-formation capacity by miR-26b was significantly reversed by cotransfection of YAF2 3′ UTR but not of YAF2 3′ UTR-mut-both (Figure 7G). Similar experiments in XM322 reflected the same results (Figure 7H). Taken together, we suggested that the circRGPD6/miR-26b/YAF2 axis plays a critical role in maintenance of a stem-like characteristic and cancer development. Therefore, TV-circRGPD6 eradicates long-term-cultured BCSCs via a miR-26b/YAF2 axis (Figure 7I).

Expression of circRGPD6 Is Positively Correlated with YAF2, and It Acts as a Favorable Prognosis of BC, whereas miR-26b Is an Unfavorable Prognostic Factor

Given the striking effect of TV-circRGPD6 treatment on metastasis and invasion of both BCSCs and BC cells, we then questioned whether there was an association between circRGPD6 expression and clinical prognosis in patients with BC. We included 5 clinical specimens with paired BC and the corresponding adjacent HBTs. Northern blot results showed that circRGPD6 was significantly reduced in tumor tissues compared to healthy tissues (Figure 8A). Notably, the linear RGPD6 mRNA expression was not changed (Figure 8A). Next, FISH analysis of circRGPD6 expressions using a biotin-labeled specific probe was performed and showed low expression of circRGPD6 in breast

Figure 6. TV-circRGPD6 Serves as a microRNA (miRNA) Sponge for miR-26b

(A) Heatmap of miRNA microarray profile to explore the potential miRNAs sponged by circRGPD6 in MCF-7.SC and XM322. (B) Pulldown assay to indicate the enrichment of TV-circRGPD6 and miR-26b-5p in MCF-7.SC and XM322. (C) Schematic diagram of circRGPD6-3′ UTR and mutation of circRGPD6-3′ UTR for the presence and absence of miR-26b-conversed binding sites. (D) Luciferase assay of HEK293T cells cotransfected with a scrambled Ctrl, miR-26b mimics, and a luciferase reporter containing wild-type (circRGPD6-WT [wild-type]) or mutant constructs with mutated miR-26b binding sites (circRGPD6-mut). (E) Luciferase assay of HEK293T cells cotransfected with Ctrl, miR-26b-LNA, and a luciferase reporter containing circRGPD6-WT or circRGPD6-mut. (F) FISH analysis of colocalization of miR-26b-5p and TV-circRGPD6 in MCF-7.SC and XM322. Scale bars, 10 μm. (G) Flow cytometry analysis of CD44$^+$CD24$^-$ expression in MCF-7.SC and XM322 following transfection of NC (negative control) plus miR-Ctrl, TV-circRGPD6 plus miR-Ctrl, NC plus miR-26b mimics, or TV-circRGPD6 plus miR-26b mimics. (H) Representative images (left panel) and quantified results (right panel) of colony formation after transfection of NC plus miR-Ctrl, TV-circRGPD6 plus miR-Ctrl, NC plus miR-26b mimics, and TV-circRGPD6 plus miR-26b mimics, respectively. Scale bars, 100 μm. Each experiment was repeated more than three times. *$p < 0.05$. Statistical analysis was performed using the paired t test.

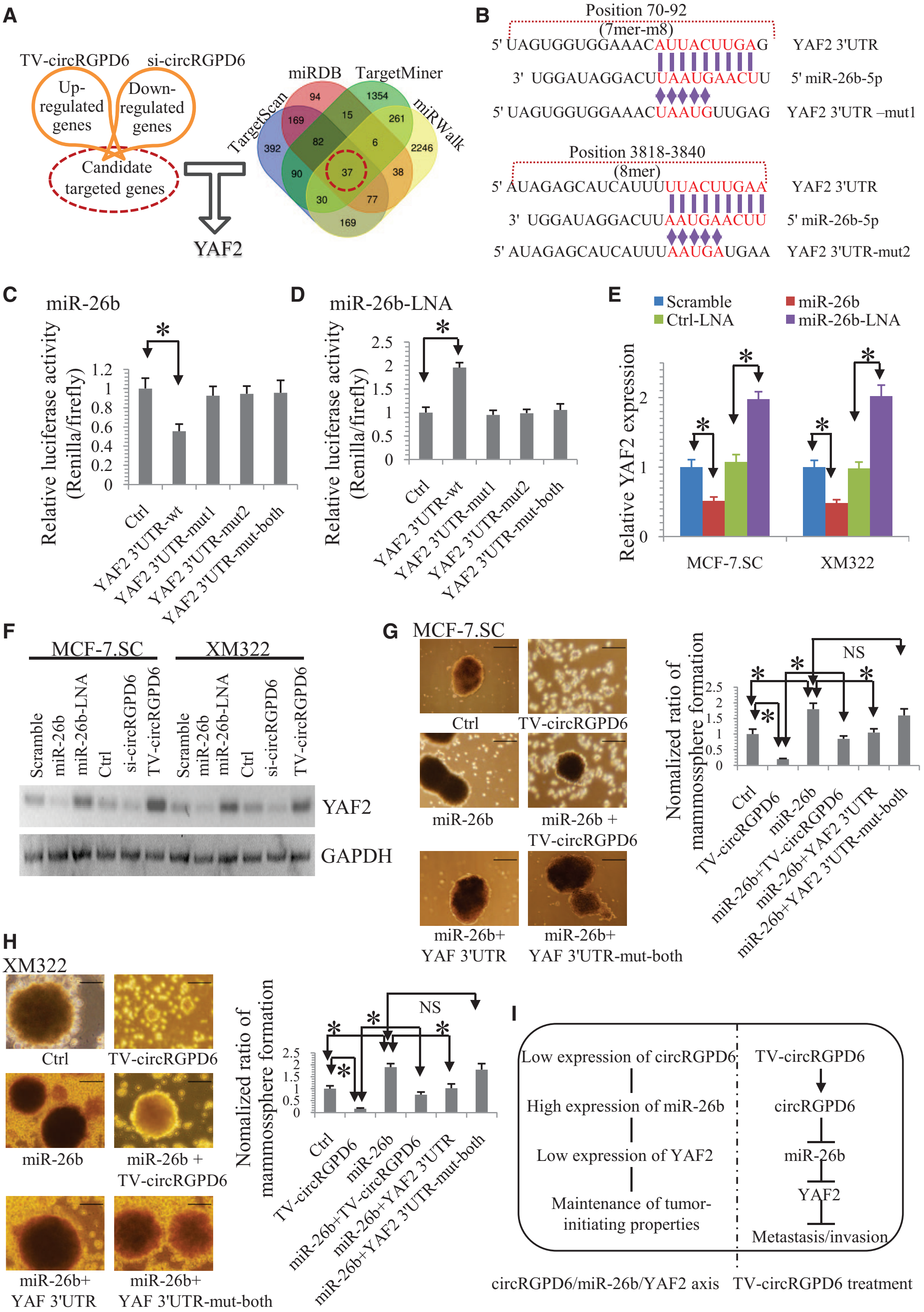

Figure 7. YAF2 Is a Direct Target Gene of miR-26b and Upregulated by TV-circRGPD6

(A) cDNA microarray profiles regulated by circRGPD6 in both MCF-7.SC and XM322; Venn diagram representing the overlap of cotarget genes of miR-26b based on four algorithms (TargetScan, miRDBDB, TargetMiner, and miRWalk). (B) Schematic diagram of YAF2 3′ UTR-WT and mutated YAF2-3′ UTR (YAF2 3′ UTR-mut) for the presence

(legend continued on next page)

tumor tissues compared to healthy tissues (Figure 8B). To further answer this question, we retrospectively analyzed clinicopathological data of 165 patients from previous reports (Table S4). Furthermore, we evaluated expressions of circRGPD6, YAF2, miR-26b, and other clinicopathological data from a retrospective database, including 165 BC tissues and 83 of the corresponding HBTs. Representative *in situ* hybridization (ISH) images of circRGPD6 expressions in both BC and HBT are presented in Figures 8C and 8D. Representative images of YAF2 expression of both BC and HBT are shown in Figures 8E and 8F. We found that expression of circRGPD6 was positive associated to YAF2 expression in BC tissue ($p < 0.001$; Table 1). Further, we evaluated expressions of circRGPD6, YAF2, miR-26b, and other clinicopathological data from a retrospective database, including 248 samples. Representative ISH images of circRGPD6 expressions in both BC and HBT are presented in Figures 8C and 8D. Representative images of YAF2 expression of both BC and HBT are shown in Figures 8E and 8F. We found that expression of circRGPD6 was positively associated to YAF2 expression in BC tissue ($p < 0.001$; Table 1). Correspondingly, HBT had a higher expression of circRGPD6 expression than breast tumor tissue in stages I–III or stage IV. Significantly, patients without metastasis showed significantly increased circRGPD6 expression in BC compared to those with metastasis ($p < 0.01$; Table 1). In addition, Kaplan-Meier survival analyses showed that BC patients with high expression of circRGPD6 had a superior rate of disease-free survival (DFS) and overall survival (OS) than those with low expression (Figure 8G). Moreover, we found a more unfavorable DFS and OS in the group that had high expression of miR-26b than those with low expression of miR-26b (Figure 8H). Further, YAF2-positive expression was significantly related with longer DFS and OS (Figure 8I). Therefore, positive expressions of circRGPD6 and YAF2 are associated with favorable prognosis in patients with BC, whereas miR-26b expression is an unfavorable prognostic factor.

DISCUSSION

In this study, we observed that the metastatic BC cell has abundant tumor-initiating biological properties, and BCSC-bearing tumors are more prone to metastasis. We also demonstrated that BCSCs mediate metastasis of BC. A microarray profile revealed that circRGPD6 is the most pronounced circRNA for further BCSC investigation. We developed TV delivery of circRGPD6, TV-circRGPD6 nanoparticle, which induces high expression of circRGPD6 in both BC cells and BCSCs. TV-circRGPD6 significantly suppressed the tumor-initiating properties of BCSCs *in vitro* and *in vivo*, as well as synergizes with docetaxel against proliferation and metastasis of BC. Furthermore, we uncovered an underlying mechanism of TV-circRGPD6 suppressing BCSC-mediated metastasis via the miR-26b/YAF2 axis. Clinical results showed that expressions of circRGPD6 and YAF2 are positively associated with the favorable outcome of BC patients, whereas miR-26b is an unfavorable prognostic factor of BC outcome. Further investigation is needed to clarify the detailed upstream regulation on circRGPD6 involved in BCSCs.

In the process of cancer metastasis, we found that disseminated tumor cells rarely originate from their primary cancer cells directly. However, BCSCs mediated BC metastasis. It is widely believed that cancer-associated EMT is not a simple process to obtain the ability for cancer cell migration and invasion[36] but a comprehensive reprogramming procedure through which differentiated epithelial cancer cells can be reversed to an undifferentiated state, not only expressing stem cell markers but also gaining stem cell-like functions.[9,37,38] In our results, BCSCs gain a wide range of differentiation potentials, which indicated that BCSCs have switched into an epithelial state or mesenchymal state. This indicated that the so-called metastasis-initiating cells likely originate from circulating CSCs with an EMT phenotype. All of these results also provided reasonable explanations for the clinical question of why protein expressions in primary tumors are frequently different than those in metastatic tumors.

circRNAs play vital roles in controlling properties of human progenitor cells.[17,19,39] Our results confirmed that circRGPD6 overexpression by TV-circRGPD6 significantly suppresses tumor-initiating properties of BCSCs *in vitro*, as well as stem-like properties of metastatic breast tumors *in vivo*. The TV system is a nonviral system that contains three basic elements: the hTERT promoter, the two-step transcriptional amplification system (GAL4-VP2), and the WPRE sequence.[7,11,13,14] TV-circRGPD6 selectively increases the expression of circRGPD6 in BCSCs proceeding with the following steps: (1) the hTERT promoter within TV can direct preferential transgene expression in BC cells and BCSCs rather than HMECs or adult stem cells;[7] (2) the hTERT promoter drives expression of the GAL4-VP2 (two copies of VP16) fusion protein; (3) GAL4-VP2 discerns the promoter G5E4T, owing to G5E4T containing five GAL4 sites positioned upstream of the adenovirus E4 TATA box; (4) G5E4T induces the expression of the circRGPD6 transcripts and then generates cirRGPD6; (5) circRGPD6 interacts with miR-26b, which regulates YAF2 expression, leading to inhibition of proliferation and metastasis of BCSCs. In summary, the TV-circRGPD6 plasmid has the appropriate construction to suppress BCSC-mediated metastasis.

and absence of miR-26b-conversed binding sites. (C) Luciferase assay of HEK293T cells cotransfected with a scrambled Ctrl, miR-26b mimics, and a luciferase reporter containing YAF2 3′ UTR-WT or YAF2 3′ UTR-mut. (D) Luciferase assay of HEK293T cells cotransfected with Ctrl, miR-26b-LNA, and a luciferase reporter containing YAF2 3′ UTR-WT or YAF2 3′ UTR-mut. (E) qRT-PCR analysis of YAF2 mRNA expressions in MCF-7.SC and XM322 after transfection with a scrambled Ctrl, miR-26b mimics, Ctrl-LNA, and miR-26b-LNA. (F) Western blot for YAF2 and GAPDH in MCF-7.SC and XM322 after treatment of miR-26b mimics, miR-26b-LNA, TV-circRGPD6, and si-circRGPD6. (G) Representative images (left panel) and statistical results (right panel) of mammosphere formation of MCF-7.SC after treatments of Ctrl, TV-circRGPD6, miR-26b, miR-26b plus TV-circRGPD6, miR-26b plus YAF2 3′ UTR, and miR-26b plus YAF2 3′ UTR-mut-both. (H) Representative images (left panel) and statistical results (right panel) of mammosphere formation of XM322 after treatments of Ctrl, TV-circRGPD6, miR-26b, miR-26b plus TV-circRGPD6, miR-26b plus YAF2 3′ UTR, and miR-26b plus YAF2 3′ UTR-mut-both. Scale bars, 100 μm. (I) Schematic illustration of TV-circRGPD6 eradicates metastasis of BCSCs via the miR-26b/YAF2 axis. Each experiment was repeated at least three times. $^*p < 0.05$; NS, not significant. Statistical analysis was performed using the paired t test.

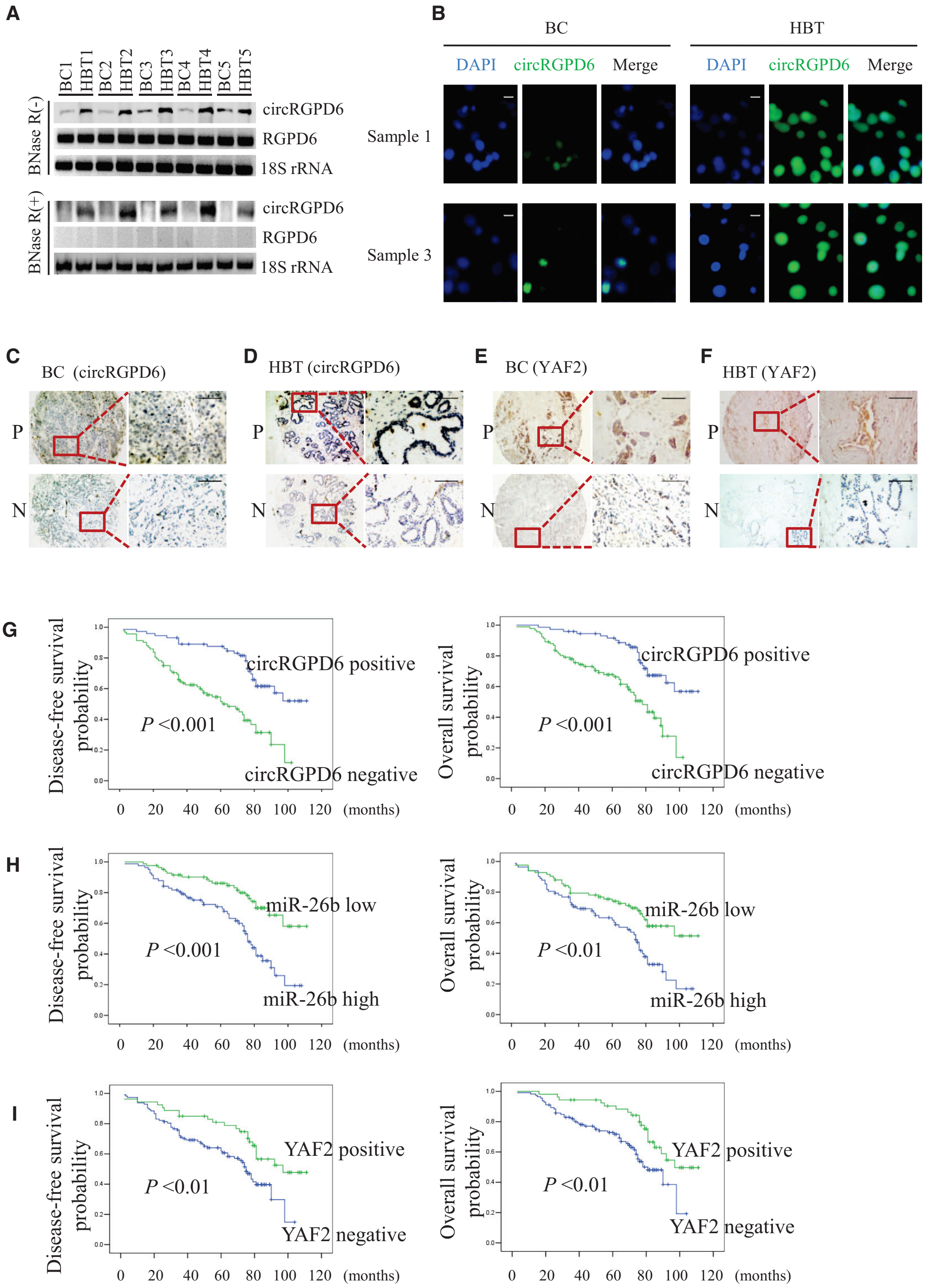

(legend on next page)

Table 1. Distributions of circRGPD6 Expressions among Breast Cancer Tissues (Stages I–III/without Metastasis and Stage IV/with Metastasis), Healthy Breast Tissues (HBTs), and YAF2 Status

		circRGPD6 Status		
Different Tissues	Total n (%)	Negative n (%)	Positive n (%)	p Value
YAF2 Status				<0.001
Negative	160 (100)	104 (65.0)	56 (35.0)	
Positive	88 (100)	20 (22.7)	68 (77.3)	
Pathological Staging				<0.01
HBT	83 (100)	37 (44.6)	46 (55.4)	
Stages I–III/without metastasis	134 (100)	62 (46.3)	72 (53.7)	
Stage IV/with metastasis	31 (100)	25 (80.6)	6 (19.4)	

Stat Statistical analyses were performed using Pearson chi-square test.

Emerging evidence indicates that circRNA RGPD6 potentially acts as a required novel biomarker and therapeutic target for cancer treatment. The circRGPD6 gene locates in chromosome 2q13, which is one of the evolutionarily conserved developmental genes in humans.[40] It has been reported that RGPD6 shares strong sequence similarity with RANBP2, a large RAN-binding protein localized at the cytoplasmic side of the nuclear pore complex.[41] RAN is a small GTP-binding protein in the RAS superfamily, which is associated with the nuclear membrane and is proposed to regulate a variety of cellular functions.[41] Recently, increasing evidence showed that the GTP-binding protein has a close association with metastasis of cancer cells.[42] Moreover, Jaiswal and his colleagues found that deletion of important developmental genes RGPD5, RGPD6, and LIMS3 in the 2q13 region may lead to rare phenotypic features of isochromosome 18p (e.g., low birth weight, microcephaly, low-set ears, strabismus, a small pinched nose, short palpebral fissures, and a small jaw) in the child.[40] In our study, we integrated the TV-circRGPD6 nanoparticle to induce high throughput of circRGPD6 expression in BCSCs, which significantly suppresses tumor-initiating properties, invasion, and metastasis of BCSCs. Thus, we revealed the potential connection among RGPD6, GTP-binding protein, and metastasis-initiating cells.

Practically, docetaxel acts as one of the standard medicines for therapy in patients with invasive BC.[43] In our study, we found that docetaxel alone played no role in eliminating tumor metastasis but synergized with TV-circRGPD6 against BCSC-mediated metastasis. Furthermore, we performed clonal pair-cell analyses to show that TV-circRGPD6 could decrease stem-like marker CD44 expression and increase DNA damage marker p-H2AX expression in BCSCs. All of these results demonstrated that TV-circRGPD6 sensitizes BCSC-mediated metastasis to docetaxel by damaging DNA of BCSCs. From *in vivo* experiments, we also found that the suppression of the $CD44^+CD24^-$ CSC population by TV-circRGPD6 alone or plus docetaxel is insufficient to evidence the inhibition of proliferation and metastasis in BCSCs. It cannot rule out that the proliferation and metastasis in BCSC-bearing tumors were influenced by not only the $CD44^+CD24^-$ CSC population but also the capability of pluripotency differentiation, microenvironment, and immunologic function, etc.[44–47] Nevertheless, these results still strongly suggested that circRGPD6 overexpression eliminates BCSCs, especially combining the usage of docetaxel chemotherapy. Therefore, TV-circRGPD6 therapy provides a potential avenue to protect against tumor metastasis.

In conclusion, we have successfully constructed the biological rationale of association between the metastatic model and stemness of BC. We also developed the nonviral TV-circRGPD6 nanoparticle, which has strong potential to be used as a clinical application in metastatic BC therapy targeting BCSC-mediated metastasis.

MATERIALS AND METHODS

Patients, Tissues, Tissue Microarray Construction (TMA), and IHC

Informed consent was obtained from all patients. All animal studies and related experiments were approved by the Research Ethics Committee of Sun Yat-sen University Cancer Center (SYSUCC). A total amount of 191 female patients with BC hospitalized in SYSUCC from October 2001 to September 2013 were enrolled in our cohort. A complete patient follow-up was performed, and endpoint of this follow-up was August 2017. Expression data were obtained from 248 fresh-frozen resected breast specimens consisting of 165 tumor tissues and 83 adjacent normal breast tissues. The remaining experimental procedures can be found in Supplemental Information.

Cell Culture

BCSCs were maintained as spheres in ultralow attachment cell-culture flasks in serum-free DMEM-F12 and supplemented with 10 ng/mL basic fibroblast growth factor (BFGF), 20 ng/mL EGF, 2% B27, 5 μg/mL insulin, and 10,000 IU/mL penicillin-streptomycin. See Supplemental Information for details on data processing.

Figure 8. Positive Expressions of Both circRGPD6 and YAF2 Are Correlated with Favorable Prognosis in Patients with BC, whereas miR-26b Expression Is an Unfavorable Marker

(A) Northern blot for circRGPD6 expression in 5 paired BC tumor tissues and their corresponding adjacent healthy breast tissues (HBTs). circRGPD6 was detected using a back-splice junction probe. RGPD6 mRNA was detected using a RGPD6-specific probe. 18S was a loading control, and RNA samples for 18S detection were not treated with RNase R. (B) FISH analysis of circRGPD6 expression in BC samples #1 and #3. Scale bars, 10 μm. (C and D) Representative *in situ* hybridization images of circRGPD6 in BC (C) and HBT (D). Positive staining is shown at the top, and negative is shown at the bottom. (E and F) Representative images of IHC for YAF2 in BC (E) and HBT (F). Positive staining is at the top, and negative is at the bottom. (G–I) Kaplan-Meier survival curves of disease-free survival (left panel) and overall survival (right panel) for circRGPD6 *in situ* hybridization expression (G), miR-26b expression, "miR-26b low" refers to values less than median; "miR-26b high" refers to values more than median. (H), and YAF2 expression (I) in BC. Scale bars, 100 μm. $^*p < 0.05$. Statistical analysis was performed using the log rank test.

Tumor Transplantation Experiments

To test tumorigenesis abilities of BCSCs *in vivo*, we established orthotopic xenograft models of BCSCs and unsorted parent cells coming from clinical samples. NOD/SCID mice were raised in a specific pathogen-free environment according to the institutional policy. Tumor progression was evaluated daily using the *In Vivo* Imaging System (IVIS system) equipped with Living Imaging software. The secretion concentrations of cytokines (TNF-α, IL-6, and IFN-γ) in mouse sera were quantified using the Cytometric Bead Array (CBA) Kit for mouse inflammatory cytokines (BD Biosciences). The test was repeated more than five times. See also Supplemental Information.

Microarray Analyses of mRNA Expression Profiles

RNA extraction and microarray analysis total RNA from BCSCs transfected with TV-circRGPD6 and si-circRGPD6 for 48 h were extracted using Trizol reagent. Synthesis of cDNA was performed using the SuperScript Choice System according to the manufacturer's protocol (Invitrogen Life Technologies, Capital Biochip). These results have been submitted to ArrayExpress (accession numbers E-MTAB-5584, E-MTAB-7556, and E-MTAB-7557). Details are available in Supplemental Information.

Statistical Analyses

All statistical analyses were performed using the SPSS 22.0 software package (SPSS, Chicago, IL, USA). Mean ± standard deviation (SD) was used to present quantitative data. For comparisons, Mann-Whitney U test, paired t test, Pearson chi-square test, Pearson correlation analysis, Fisher's exact test, and log rank test were performed as indicated. Survival rates were analyzed by log rank test. The significance level was set at $p < 0.05$. All data in our study have been recorded at SYSUCC for future reference (number RDDB2020000967RDD).

SUPPLEMENTAL INFORMATION

Supplemental Information can be found online at https://doi.org/10.1016/j.ymthe.2020.09.005.

AUTHOR CONTRIBUTIONS

X.X. and X.L. conceived the study, designed experiments, and wrote the manuscript. X.L. had full access to execute and analyze the experiments. F.W., W.C., X.X., and X.L. participated in respective experiments.

CONFLICTS OF INTEREST

The authors declare no competing interests.

ACKNOWLEDGMENTS

The authors would like to thank all patients who provided samples for the study. This work was supported by funds from the National Natural Science Foundation of China (81672598 and 81872152); China Postdoctoral Science Foundation (2017M610570); Natural Science Foundation of Guangdong (2013B060300009); Science and Technology Planning Project of Guangzhou (2014J4100169); Guiding Project of Science and Technology Department of Fujian Province (2016Y0020); Training Project Funding Plan of Young and Middle-aged Talent of Health System in Fujian Province (2016-ZQN-18); Training Project Funding Plan of Youth Innovative Talents of Fujian Provincial Maternity and Children's Hospital (YCXB 18-01); and Sisters Hospital Network Fund (SINF) between University of Texas MD Anderson Cancer Center and Sun Yat-sen University Cancer Center.

REFERENCES

1. Adorno-Cruz, V., Kibria, G., Liu, X., Doherty, M., Junk, D.J., Guan, D., Hubert, C., Venere, M., Mulkearns-Hubert, E., Sinyuk, M., et al. (2015). Cancer stem cells: targeting the roots of cancer, seeds of metastasis, and sources of therapy resistance. Cancer Res. *75*, 924–929.
2. Bray, F., Ferlay, J., Soerjomataram, I., Siegel, R.L., Torre, L.A., and Jemal, A. (2018). Global cancer statistics 2018: GLOBOCAN estimates of incidence and mortality worldwide for 36 cancers in 185 countries. CA Cancer J. Clin. *68*, 394–424.
3. Ye, X., and Weinberg, R.A. (2015). Epithelial-Mesenchymal Plasticity: A Central Regulator of Cancer Progression. Trends Cell Biol. *25*, 675–686.
4. Jeong, K.Y., Lee, E.J., Kim, S.J., Yang, S.H., Sung, Y.C., and Seong, J. (2015). Irradiation-induced localization of IL-12-expressing mesenchymal stem cells to enhance the curative effect in murine metastatic hepatoma. Int. J. Cancer *137*, 721–730.
5. Lytle, N.K., Ferguson, L.P., Rajbhandari, N., Gilroy, K., Fox, R.G., Deshpande, A., Schürch, C.M., Hamilton, M., Robertson, N., Lin, W., et al. (2019). A Multiscale Map of the Stem Cell State in Pancreatic Adenocarcinoma. Cell *177*, 572–586.e22.
6. Calvanese, V., Nguyen, A.T., Bolan, T.J., Vavilina, A., Su, T., Lee, L.K., Wang, Y., Lay, F.D., Magnusson, M., Crooks, G.M., et al. (2019). MLLT3 governs human haematopoietic stem-cell self-renewal and engraftment. Nature *576*, 281–286.
7. Lin, X., Chen, W., Wei, F., Zhou, B.P., Hung, M.C., and Xie, X. (2017). Nanoparticle Delivery of miR-34a Eradicates Long-term-cultured Breast Cancer Stem Cells via Targeting C22ORF28 Directly. Theranostics *7*, 4805–4824.
8. Lin, X., Chen, W., Wei, F., Zhou, B.P., Hung, M.C., and Xie, X. (2017). POMC maintains tumor-initiating properties of tumor tissue-derived long-term-cultured breast cancer stem cells. Int. J. Cancer *140*, 2517–2525.
9. Li, L., and Li, W. (2015). Epithelial-mesenchymal transition in human cancer: comprehensive reprogramming of metabolism, epigenetics, and differentiation. Pharmacol. Ther. *150*, 33–46.
10. Mahvi, D.A., Liu, R., Grinstaff, M.W., Colson, Y.L., and Raut, C.P. (2018). Local Cancer Recurrence: The Realities, Challenges, and Opportunities for New Therapies. CA Cancer J. Clin. *68*, 488–505.
11. Xie, X., Xia, W., Li, Z., Kuo, H.P., Liu, Y., Li, Z., Ding, Q., Zhang, S., Spohn, B., Yang, Y., et al. (2007). Targeted expression of BikDD eradicates pancreatic tumors in noninvasive imaging models. Cancer Cell *12*, 52–65.
12. Lang, J.Y., Hsu, J.L., Meric-Bernstam, F., Chang, C.J., Wang, Q., Bao, Y., Yamaguchi, H., Xie, X., Woodward, W.A., Yu, D., et al. (2011). BikDD eliminates breast cancer initiating cells and synergizes with lapatinib for breast cancer treatment. Cancer Cell *20*, 341–356.
13. Li, L., Xie, X., Luo, J., Liu, M., Xi, S., Guo, J., Kong, Y., Wu, M., Gao, J., Xie, Z., et al. (2012). Targeted expression of miR-34a using the T-VISA system suppresses breast cancer cell growth and invasion. Mol. Ther. *20*, 2326–2334.
14. Xie, X., Li, L., Xiao, X., Guo, J., Kong, Y., Wu, M., Liu, W., Gao, G., Hsu, J.L., Wei, W., et al. (2012). Targeted expression of BikDD eliminates breast cancer with virtually no toxicity in noninvasive imaging models. Mol. Cancer Ther. *11*, 1915–1924.
15. Günes, C., and Rudolph, K.L. (2013). The role of telomeres in stem cells and cancer. Cell *152*, 390–393.
16. Errichelli, L., Dini Modigliani, S., Laneve, P., Colantoni, A., Legnini, I., Capauto, D., Rosa, A., De Santis, R., Scarfò, R., Peruzzi, G., et al. (2017). FUS affects circular RNA expression in murine embryonic stem cell-derived motor neurons. Nat. Commun. *8*, 14741–14751.
17. Kristensen, L.S., Okholm, T.L.H., Venø, M.T., and Kjems, J. (2018). Circular RNAs are abundantly expressed and upregulated during human epidermal stem cell differentiation. RNA Biol. *15*, 280–291.

18. Zheng, Y., Li, X., Huang, Y., Jia, L., and Li, W. (2017). The Circular RNA Landscape of Periodontal Ligament Stem Cells During Osteogenesis. J. Periodontol. *88*, 906–914.

19. Yu, C.Y., Li, T.C., Wu, Y.Y., Yeh, C.H., Chiang, W., Chuang, C.Y., and Kuo, H.C. (2017). The circular RNA circBIRC6 participates in the molecular circuitry controlling human pluripotency. Nat. Commun. *8*, 1149–1153.

20. Zhang, K., Che, S., Su, Z., Zheng, S., Zhang, H., Yang, S., Li, W., and Liu, J. (2018). CD90 promotes cell migration, viability and sphere-forming ability of hepatocellular carcinoma cells. Int. J. Mol. Med. *41*, 946–954.

21. Hosseini, H., Obradović, M.M.S., Hoffmann, M., Harper, K.L., Sosa, M.S., Werner-Klein, M., Nanduri, L.K., Werno, C., Ehrl, C., Maneck, M., et al. (2016). Early dissemination seeds metastasis in breast cancer. Nature *540*, 552–558.

22. Hanniford, D., Ulloa-Morales, A., Karz, A., Berzoti-Coelho, M.G., Moubarak, R.S., Sánchez-Sendra, B., Kloetgen, A., Davalos, V., Imig, J., Wu, P., et al. (2020). Epigenetic Silencing of CDR1as Drives IGF2BP3-Mediated Melanoma Invasion and Metastasis. Cancer Cell *37*, 55–70.e15.

23. Li, J.H., Liu, S., Zhou, H., Qu, L.H., and Yang, J.H. (2014). starBase v2.0: decoding miRNA-ceRNA, miRNA-ncRNA and protein-RNA interaction networks from large-scale CLIP-Seq data. Nucleic Acids Res. *42*, D92–D97.

24. Dudekula, D.B., Panda, A.C., Grammatikakis, I., De, S., Abdelmohsen, K., and Gorospe, M. (2016). CircInteractome: A web tool for exploring circular RNAs and their interacting proteins and microRNAs. RNA Biol. *13*, 34–42.

25. Cao, Y., Huschtscha, L.I., Nouwens, A.S., Pickett, H.A., Neumann, A.A., Chang, A.C., Toouli, C.D., Bryan, T.M., and Reddel, R.R. (2008). Amplification of telomerase reverse transcriptase gene in human mammary epithelial cells with limiting telomerase RNA expression levels. Cancer Res. *68*, 3115–3123.

26. Marquardt, S., Solanki, M., Spitschak, A., Vera, J., and Pützer, B.M. (2018). Emerging functional markers for cancer stem cell-based therapies: Understanding signaling networks for targeting metastasis. Semin. Cancer Biol. *53*, 90–109.

27. Merino, D., Whittle, J.R., Vaillant, F., Serrano, A., Gong, J.N., Giner, G., Maragno, A.L., Chanrion, M., Schneider, E., Pal, B., et al. (2017). Synergistic action of the MCL-1 inhibitor S63845 with current therapies in preclinical models of triple-negative and HER2-amplified breast cancer. Sci. Transl. Med. *9*, 7049–7059.

28. Lu, Y., Yue, Z., Xie, J., Wang, W., Zhu, H., Zhang, E., and Cao, Z. (2018). Micelles with ultralow critical micelle concentration as carriers for drug delivery. Nat. Biomed. Eng. *2*, 318–325.

29. Manshian, B.B., Pfeiffer, C., Pelaz, B., Heimerl, T., Gallego, M., Möller, M., del Pino, P., Himmelreich, U., Parak, W.J., and Soenen, S.J. (2015). High-Content Imaging and Gene Expression Approaches To Unravel the Effect of Surface Functionality on Cellular Interactions of Silver Nanoparticles. ACS Nano *9*, 10431–10444.

30. Huang, H.C., Pigula, M., Fang, Y., and Hasan, T. (2018). Immobilization of Photo-Immunoconjugates on Nanoparticles Leads to Enhanced Light-Activated Biological Effects. Small *1*, e1800236.

31. Glažar, P., Papavasileiou, P., and Rajewsky, N. (2014). circBase: a database for circular RNAs. RNA *20*, 1666–1670.

32. Agarwal, V., Bell, G.W., Nam, J.W., and Bartel, D.P. (2015). Predicting effective microRNA target sites in mammalian mRNAs. eLife *4*, 5005–5042.

33. Wong, N., and Wang, X. (2015). miRDB: an online resource for microRNA target prediction and functional annotations. Nucleic Acids Res. *43*, D146–D152.

34. Bandyopadhyay, S., and Mitra, R. (2009). TargetMiner: microRNA target prediction with systematic identification of tissue-specific negative examples. Bioinformatics *25*, 2625–2631.

35. Dweep, H., and Gretz, N. (2015). miRWalk2.0: a comprehensive atlas of microRNA-target interactions. Nat. Methods *12*, 697.

36. Lamouille, S., Xu, J., and Derynck, R. (2014). Molecular mechanisms of epithelial-mesenchymal transition. Nat. Rev. Mol. Cell Biol. *15*, 178–196.

37. Harries, M.J., Jimenez, F., Izeta, A., Hardman, J., Panicker, S.P., Poblet, E., and Paus, R. (2018). Lichen Planopilaris and Frontal Fibrosing Alopecia as Model Epithelial Stem Cell Diseases. Trends Mol. Med. *24*, 435–448.

38. Tam, W.L., and Weinberg, R.A. (2013). The epigenetics of epithelial-mesenchymal plasticity in cancer. Nat. Med. *19*, 1438–1449.

39. Hansen, T.B., Kjems, J., and Damgaard, C.K. (2013). Circular RNA and miR-7 in cancer. Cancer Res. *73*, 5609–5612.

40. Jaiswal, S.K., Kumar, A., Ali, A., and Rai, A.K. (2015). Co-occurrence of mosaic supernumerary isochromosome 18p and intermittent 2q13 deletions in a child with multiple congenital anomalies. Gene *559*, 94–98.

41. Neilson, D.E., Adams, M.D., Orr, C.M., Schelling, D.K., Eiben, R.M., Kerr, D.S., Anderson, J., Bassuk, A.G., Bye, A.M., Childs, A.M., et al. (2009). Infection-triggered familial or recurrent cases of acute necrotizing encephalopathy caused by mutations in a component of the nuclear pore, RANBP2. Am. J. Hum. Genet. *84*, 44–51.

42. Jansen, S., Gosens, R., Wieland, T., and Schmidt, M. (2018). Paving the Rho in cancer metastasis: Rho GTPases and beyond. Pharmacol. Ther. *183*, 1–21.

43. Bowerman, C.J., Byrne, J.D., Chu, K.S., Schorzman, A.N., Keeler, A.W., Sherwood, C.A., Perry, J.L., Luft, J.C., Darr, D.B., Deal, A.M., et al. (2017). Docetaxel-Loaded PLGA Nanoparticles Improve Efficacy in Taxane-Resistant Triple-Negative Breast Cancer. Nano Lett. *17*, 242–248.

44. Shi, X., Zhang, X., Li, J., Mo, L., Zhao, H., Zhu, Y., Hu, Z., Gao, J., and Tan, W. (2018). PD-1 blockade enhances the antitumor efficacy of GM-CSF surface-modified bladder cancer stem cells vaccine. Int. J. Cancer *142*, 2106–2117.

45. Saygin, C., Matei, D., Majeti, R., Reizes, O., and Lathia, J.D. (2019). Targeting Cancer Stemness in the Clinic: From Hype to Hope. Cell Stem Cell *24*, 25–40.

46. Rodríguez, M.M., Fiore, E., Bayo, J., Atorrasagasti, C., García, M., Onorato, A., Domínguez, L., Malvicini, M., and Mazzolini, G. (2018). 4Mu Decreases CD47 Expression on Hepatic Cancer Stem Cells and Primes a Potent Antitumor T Cell Response Induced by Interleukin-12. Mol. Ther. *26*, 2738–2750.

47. Lo Re, O., Mazza, T., Giallongo, S., Sanna, P., Rappa, F., Vinh Luong, T., Li Volti, G., Drovakova, A., Roskams, T., Van Haele, M., et al. (2020). Loss of histone macroH2A1 in hepatocellular carcinoma cells promotes paracrine-mediated chemoresistance and CD4$^+$CD25$^+$FoxP3$^+$ regulatory T cells activation. Theranostics *10*, 910–924.

YMTHE, Volume *29*

Supplemental Information

TV-circRGPD6 Nanoparticle Suppresses Breast Cancer Stem Cell-Mediated Metastasis via the miR-26b/YAF2 Axis

Xiaoti Lin, Weiyu Chen, Fengqin Wei, and Xiaoming Xie

SUPPLEMENTAL INFORMATION

Supplemental Experimental Procedures

Supplementary Tables S1-4

Supplementary Figures S1-7

Supplemental Experimental Procedures

Patients and animal studies

Informed consent was obtained from all patients. All animal experiments and related studies were approved by the research ethics committee of Sun Yat-sen University Cancer Center (SYSUCC).

Cell culture and transfection procedure of breast cancer stem cells (BCSC)

Tumor tissue-derived BCSC (XM322 and XM607) were isolated by fluorescence-activated cell sorting (FACS) as previously described. [1] Cell line-derived BCSC (MDA-MB-231.SC and MCF-7.SC) were purified by magnetic-activated cell sorting (MACS). [2] The application of culture medium was as described previously. BCSC were maintained as spheres in ultralow attachment flasks in serum-free DMEM-F12 and supplemented with 10 ng/mL basic fibroblast growth factor (BFGF), 20 ng/mL epidermal growth factor (EGF), 2% B27, 5 µg/mL insulin, and 10000 IU/mL penicillin-streptomycin. BCSC were maintained as spheres in ultralow attachment flasks in serum-free DMEM-F12 and supplemented with 10 ng/mL basic fibroblast growth factor (BFGF), 20 ng/mL epidermal growth factor (EGF), 2% B27, 5 µg/mL insulin, and 10000 IU/mL penicillin-streptomycin. For preparing of single cell suspensions, BCSC were digested by TrypLE™ Express for 9 min. To establish adherent cells in differentiation culture, we added 0.50% bovine serum albumin to nutrient solution for 12 days.

MDA-MB-231, MCF-7, MDA-MB-468 and SK-br-3 breast cancer cell lines, and immortalized normal mammary epithelial cell lines (MCF-12A, 184A1) were all purchased from American Type Culture Collection (ATCC). All cell lines were cultured according to the vendor’s instructions. Briefly, the breast cancer cells were maintained under DMEM medium supplemen-ted with 10% fetal bovine serum (FBS, GIBCO, Campinas, Brazil). Immortalized normal mammary epithelial cells were raised under Mammary Epithelium Basal Medium (Clonetics, Walkersville, MD). All cells were bred at 37°C in a 5% CO_2 incubator.

Cholesterol and 1, 2-bis(oleoyloxy)-3-(trimethyl ammonio) propane (DOTAP; Avanti Polar Lipids, Alabaster, AL), were extruded and DOTAP: cholesterol liposomes were performed according to the protocol. Briefly, to evaluate the inhibitory effects on BCSC, the cells were transiently cotransfected in 24-well plates with 1mg of the TV plasmid DNA plus 0.1mg of CMV-Luc DNA using extruded DOTAP:cholesterol liposomes at an N/P ratio of 2:1 secons.

Patients, tissues, tissue microarray construction (TMA), immunohistochemistry (IHC) and *in situ* hybridization (ISH)

A total of 1691 female patients with breast cancer who hospitalized in SYSUCC from October 2001 to September 2013 were enrolled in our study. A complete patient follow-up was performed, and endpoint of this follow-up was August 2017. Expression data were obtained from 248 fresh-frozen resected breast specimens consisting of 165 tumor tissues and 83 adjacent normal breast tissues. Antibodies of YAF2 (1: 100) was performed. A total of 12 mouse tissues were involved in analyzing of IHC expressions. The primary antibodies included ER (1:50), PR (1:500), HER2 (1:50), Ki-67 (1:100), E-Cadherin (1:100), α-SMA (1:200), and Muc1 (1:50). The circRGPD6 detection probe was used for *in situ* hybridization (ISH) according to manufacturer’s protocol (Exiqon, Vedbaek, Denmark). In addition, staining procedures were performed by using Bench Mark XT automated IHC/ISH slide staining system.

Protocols of fluorescence in situ hybridization (FISH) were as follow. Briefly, hybridization was performed overnight with circRGPD6 probes. Specimens were analyzed using a Nikon inverted fluorescence microscope. The circRGPD6 probe for FISH is 5′-TTGAAGCCAGGTAGTGAAAG-3′. This assay was repeated three times.

We graded IHC/ISH status based on the combination synthetical evaluation of quantity and intensity of positive cells. Briefly, staining intensity index was grouped into four grades: negative-0 point, weak-1 point, moderate-2 points, and strong-3 points. Percentage of positive cells was segmented into 5 ranks: 0 point (0%), 1 point (1% ~ 24%), 2 points (25% ~ 49%), 3 points (50% ~ 74%), and 4 points (75% ~ 100%). The total score of both determined the status of YAF2 expression: negative (0 ~ 3 points) and positive (≥ 4 points).

In addition, we randomly analyzed of circRGPD6 expression in 22 clinical samples with breast cancer and their adjacent healthy breast tissue samples. The specimens obtained from female patients who hospitalized in SYSUCC from January

2015 to May 2015.

RNA isolation and quantitative RT-PCR (qRT-PCR)

Total RNA was extracted from flash-frozen tissue samples or cultured cells using TRIzol Reagent (Invitrogen), according to the manufacturer’s instructions. For RNA retro-transcription, the SuperScript VILO cDNA Synthesis Kit was performed (Thermo Fisher Scientific). For the detection of circRNAs and their linear counterparts, cDNA samples were analysed by quantitative real-time PCR using PowerUp SYBR Green Master Mix (Thermo Fisher Scientific). For the RNA extracted in CLIP experiments, quantitative real-time PCR was performed on cDNAs using MyTaq Red DNA Polymerase (Bioline) according to the manufacturer’s instructions. The samples were then loaded on a 2.5% agarose gel. All the images were captured using the Molecular Imager ChemiDoc XRS + (Bio-Rad), and the densitometric analyses were performed using the associated Image Lab software (Bio-Rad). Each sample was analyzed at least in triplicate.

Reverse transcription PCR

Reverse transcription for mRNA and circRNAs was performed with an MMLV-RT kit (Takara, Mountain View, CA) using random hexamers according to the manufacturer’s protocols. PCR was subsequently performed with a 1:10 dilution of reverse-transcribed cDNA. The PCR product was run in a 2% agarose gel. Quantitative real-time reverse transcription polymerase chain reactions were performed on a 7500 Real-time PCR System (Applied Biosystems, Carlsbad, CA, USA) with Universal SYBR Green Master Mix (4,913,914,001, Roche, Shanghai, China). Meanwhile, we used 18s rRNA as the internal references for circRNA.

Pull down assay

A total of 1×10^7 BCSC were harvested, lysed and sonicated. The TV-circRGPD6 probe was used for incubation with C-1 magnetic beads (Life Technologies) at 25 °C for 2 hr to generate probe-coated beads. Cell lysate with TV-circRGPD6 probe or oligo probe was incubated at 4 °C for one night. After washing with wash buffer, the RNA mix bound to the beads was eluted and extracted with an RNeasy Mini Kit (QIAGEN) for RT–PCR or real-time PCR.

Oligonucleotide transfection

The human breast cell lines MCF-7.SC and XM322 were seeded in a 6-well plate and incubated at 37 °C in humidified 5% CO2 atmosphere overnight. CircRGPD6 siRNA, miRNA mimics and inhibitors (RiboBio, Guangzhou, China) were transfected by Lipofectamine RNAiMax (Life Technologies) according to the manufacturer’s protocol.

Northern blot analysis

Digoxin-labeled DNA probes (351 nt), spanning the back-splice junction of circRGPD6, were prepared from cDNA using PCR DIG Probe Synthesis Kit (Roche, Mannheim, Germany). Total RNA (10 μg) denatured in formaldehyde was resolved on 1% agarose-formaldehyde gel and transferred onto a Hybond-N+ nylon membrane (Buckinghamshire, UK). Membranes were crosslinked, pre-hybridized in DIG Easy Hyb (Roche), following hybridized with DIG-labeled DNA probes overnight. After stringent washing, the membranes were incubated with alkaline phosphatase (AP)-conjugated anti-DIG antibodies (Roche). Immunoreactive bands were visualized using chemiluminescent substrate CSPD (Roche) followed by exposure to X-ray film.

Clonal pair-cell analysis

In brief, MCF-7.SC and XM322 (5×10^6) cells were transfected with GFP-labeled TV-circRGPD6 plasmid for 48 h, stained with 2 µL DAPI (10 µg/mL) for 5 min, and counterstained with anti-CD44-PE (1:200) for 30 min, respectively. Initially, GFP-labeled BCSC were purified and collected. Next, images were acquired by an inverted epifluorescence microscope system and further analyzed by digital confocal microscopy. Similarly, while we evaluated the association of loss of CD44 and p-H2AX expression in BCSC, clonal pair-cell analysis was performed. In brief, MCF-7.SC and XM322 (5×10^6) cells were transfected with GFP-labeled p-H2AX plasmid for 48 h, stained with 2 µL DAPI (10 µg/mL) for 5 min, and counterstained with anti-CD44-PE (1:200) for 30 min, respectively. Preliminarily, GFP-labeled BCSC were purified and collected. Next, images were acquired by an inverted epifluorescence microscope system and further analyzed by digital confocal microscopy.

Western blot analysis

Protein extracts of BCSC (10μg protein) were detached by 10 % SDS-PAGE and electrophoretically transferred to polyvinylidene difluoride (PVDF) membrane. Following, antibodies were assayed. Antibodies of CD44, Vimentin, E-cadherin, N-cadherin, HIF-1α and YAF2 were purchased from Cell Signaling Technology. We performed GAPDH as internal control. Signals were visualized using the Supersignal West Pico ECL chemiluminescence detection kit and Kodak X-ray film.

Flow cytometry

Fluorescence-activated cell sorting (FACS) was performed to determine the $CD44^+CD24^-$ subpopulation, and proportion of Lin or ALDH1 in BCSC by using $CD44^+$, $CD24^-$, Lin-PE and ALDH1-PE antibodies (Sigma). To develop adherent cells in differentiation culture, we added 0.50% bovine serum albumin to nutrient solution for 12 days. Differentiation capabilities of BCSC were further analyzed by flow cytometry. Briefly, BCSC (5×10^7 cells) were incubated with Muc1-PE or α-SMA-PE antibody for 48 hr (Sigma). Positive GFP-labeled cells were purified by FACS. Then, isolated cells were contained with 2 μl DAPI (10 μg/mL) for 5 min. We used CellQuest software to analyze the data.

Clonogenicity assays in soft agarose

Clonal expansion ability of BCSC was analyzed by clonogenicity assays in soft agarose. Briefly, BCSC were transfected with Negative Ctrl (NC) plus miR-Ctrl, TV-circRGPD6 plus miR-Ctrl, NC plus miR-26b and TV-circRGPD6 plus miR-26b, respectively. Next, 2% solidified agar was paved as base agar in 6-well. BCSC were seeded at 3×10^3 cells per well coated with a thin layer of 1% soft agarose. The experiment was terminated at day 21, and wells were Giemsa-stained. Spheres with 50 μm or greater in diameter were determined. We performed all experiments for three times.

Establishment of serial passages of luciferase-labeled and green fluorescent protein (GFP)-labeled BCSC lineages

Protocol of serial passages of cell lines expressing firefly luciferase was previously described.[1-3] Briefly, BCSC were transfected with pEF1a-Luc-Neo, and filtrated with G418 for 14 days. Next, G418-resistant clones, referred as luciferase-labeled BCSC, were collected and maintained for further *in vivo* experiments. Similarly, BCSC were transfected with pcDNA3.1-EGFP-NEO plasmid. Then GFP-labeled BCSC were selected out with G418 for 14 days. Following, GFP expression and survival BCSC were cultured. Here, G418-resistant clones were designated as GFP-labeled BCSC.

Determination of synergistic effects of TV-circRGPD6 and docetaxel

GFP-labeled BCSC were transfected with Ctrl, TV-circRGPD6, si-circRGPD6, docetaxe, as well as TV-circRGPD6 plus docetaxel. We used a spinning disk confocal long-term live cell imaging system (Olympus CV1000) to maintain and photograph these cells in real time. Mammospheres with 50 μm or greater in diameter were determined. For the detection of synergistic effects of TV-circRGPD6 and docetaxel, BCSC were treated with Ctrl, 2 nM docetaxel (Aventis Pharma, France), [4] presence or absence of docetaxel after 0.1 nM TV-circRGPD6 transduction during in the corresponding period (0 day, 1 day, 3 days and 5 days) respectively. GFP intensity was measured with MetaMorph image acquisition and analysis software (Molecular Devices). All experiments were repeated for five times.

MTT assay of cell proliferation

MTT (Sigma) assay was used to assess MCF-7.SC cell viability according to the manufacturer’s instructions. Each assay was repeated five times.

Terminal deoxynucleotidyl transferase-mediated dUTP nick-end labeling (TUNEL) test

TUNEL staining for apoptosis was performed using the ApopTag Plus Peroxidase In Situ Apoptosis Detection kit (Invitrogen CA, USA) according to the manufacturer’s instructions.

Constructs and transfection

Detailed information of the VISA plasmid, hTERT promoter-driven VISA nanoparticle delivery of circRGPD6 (TV-circRGPD6) were described previously. [1-3, 5-7] Briefly, the circRGPD6 shRNA was incorporated into the Bgl II/Nhe I sites of the plasmid pGL3-T-VISA-Luc; following, the T-VISA-circRGPD6 fragment of pGL3-T-VISA-circRGPD6 was subcloned into the Not I and Sal I sites of pUK21. Transient transfections were performed as previously described. [1, 2] Briefly, BCSC were transiently transfected with 1μg of the hTERT-VISA plasmid DNA using extruded DOTAP: cholesterol liposomes in 24-well plates (N/P ratio of 2:1). Silence sequence of circRGPD6: GTTGCTCAAGAGCCTCCATTA. For site-specific mutagenesis, we mutated the regions in the circRGPD6-3'UTR and YAF2-3'UTR complementary to the seed sequence of miR-26b using the QuikChange II Site-Directed Mutagenesis Kit according to manufacturer's protocol.

In the evaluation of the effect of circRGPD6/miR-26b/YAF2 axis on mammosphere formation of BCSC, both MCF-7.SC and XM322 were transfected with Ctrl, TV-circRGPD6, miR-26b, miR-26b plus TV-circRGPD6, miR-26b plus YAF2 3'UTR, and miR-26b plus YAF2 3'UTR-mut-both. We used a spinning disk confocal long-term live cell imaging system (Olympus CV1000) to maintain and photograph these cells in real time. Mammospheres with 50 µm or greater in diameter were determined. All experiments were repeated for three times.

Tumor transplantation experiments

To identify the stem-like properties of metastatic breast cancer cells, we generated orthotopic xenograft models of breast cancer MCF-7 cells. In total, MCF-7 cells were maintained in 12 athymic female non-obese diabetic/severe combined immunodeficient (NOD/SCID) mice to produce both primary tumor and dissemination for 4 weeks. Following, the stem-like properties of primary tumors were compared with their corresponding disseminated tumors.

To test early dissemination capabilities of MCF-7 *in vivo*, we generated orthotopic xenograft models of luciferase-labeled MCF-7 and their luciferase-labeled primary breast cancer cell-bearing. The details were described previously.[1-3, 5, 6, 8] Briefly, NOD/SCID mice were injected subcutaneously into the left fourth mammary gland with 1×10^5 cells primary breast cancer cells or MCF-7 using a 25-gauge needle (n = 9 mice per group). After transplantation, mice were monitored using the *In Vivo* Imaging System (*IVIS*, Xenogen, Alameda, CA) to early dissemination for 10 days. All the mice were then sacrificed and tissue was collected to characterize the capability of tumor formation.

To determine BCSC mediate breast cancer metastasis, ten luciferase-labeled BCSC-bearing mice were maintained (MCF-7.SC and XM322, 5 mice per group). All of mammosphere formation, self-renewal capacity, $CD44^+CD24^-Lin^{-/low}ALDH1^+$ expressions and pluripotency capability of early disseminated tumors in the above-mentioned 10 mice were analyzed.

With a goal of exploring the potential synergy effect of TV-circRGPD6 plasmid and docetaxel in eradicating metastasis of breast cancer cells *in vivo*, a suspension of XM322-luciferase cells (5×10^6) was inoculated at the left fourth inguinal mammary gland of NOD/SCID mice using a 30-gauge needle. Tumor formation was monitored by palpation and tumor size was measured twice per week using calipers. We developed and maintained XM322 lineages with expression of firefly luciferase for 40 days (Day 0). When the tumors developed metastatic tumors with nonsignificant expressions of firefly luciferase, the mice were noninvasively imaged using the *IVIS* In Vivo Imaging System (Xenogen, Alameda, CA) to confirm tumor growth and then randomly assigned to one of five treatment groups (n = 3 mice per group). Each group of mice received 100 µL of DNA-liposome complexes that contained liposomal (Ctrl) alone, si-circRGPD6 liposomal complexes (10 µg qod), TV-circRGPD6 liposomal complexes (10 µg qod), doxetaxel (10 mg/kg qod for 5 times) alone, and TV-circRGPD6 liposomal complexes (10 µg qod) plus doxetaxel (10 mg/kg qod for 5 times), respectively. Tumor progression was monitored daily using the IVIS system. The luciferase test was performed for the following 20 days (Day 20) investigation and then the data were analyzed. Fine needle aspirations on mice were done according to standard cytopathologic practice under inhaled general anesthesia (isofluorane) using 10-mL syringes and 25-gauge needles. Fine needle aspirations were done at baseline for all mice and after 20 days of therapy for each of the primary tumors, disseminated tumor and disseminated tumor. Quantitative RT-PCR of circRGPD6 expression, FACS analysis $CD44^+CD24^-$ subpopulation and determination of firefly luciferase of BCSC-bearing tumors were performed according to manufacturer's protocol. Each experiment was repeated more than three times.

To evaluate the safety conditions of circRGPD6 treatment to BCSC *in vivo*, a suspension of XM322 cells (1×10^4) was inoculated at the left fourth inguinal mammary gland of NOD/SCID mice. When the tumors reached to ~50 mm^3, the mice were non-invasively imaged using the *In Vivo* Imaging System (IVIS, Xenogen, Alameda, CA) to monitor tumor growth. Then, all mice were randomly divided into three treatment groups (10 mice per group). Each group of mice received 100 µL of DNA-liposome complexes that contained TV-circRGPD6 liposomal complexes (10 µg qod), si-circRGPD6 liposomal complexes (10 µg qod) or liposomal (Ctrl) alone. The secretion levels of serum alanine transaminase (ALT), aspartate transaminase

(AST), blood urea nitrogen (BUN) and creatinine (Cr) were determined with an automatic analyzer (Roche Cobas Mira Plus; Roche, Mannheim, Germany). Mouse serum cytokines (TNF-α, IL-6 and IFN-γ) were quantified using the cytometric bead array kit (CBA; BD Biosciences). The test was repeated more than five times.

We performed *in vivo* experiments to determine the ability of TV-circRGPD6 inhibiting stem-like biological properties of metastatic breast cancer. In the beginning, NOD/SCID nude mice were injected subcutaneously into the right fourth mammary gland with 5×10^6 either immortal healthy mammary epithelial 184A1 cells, primary XM322 breast cancer cells in 100ml PBS using a 30-gauge needle. Mice were monitored twice a week, tumor formation was monitored by palpation and tumor size value was measured in cubic millimeters using calipers. Tumor volume was calculated using the standard formula: tumor volume = $(\text{width}^2 \times \text{length} \times\pi)/6$. When the tumors size reached to ~50 mm^3, the mice were randomly assigned to the five treatment groups (3 mice per group): liposomal (Ctrl) alone, si-circRGPD6 liposomal complexes (10 μg qod), TV-circRGPD6 liposomal complexes (10 μg qod), doxetaxel (10 mg/kg qod for 5 times), [9] and TV-circRGPD6 liposomal complexes (10 μg qod) plus doxetaxel (10 mg/kg qod for 5 times), respectively. Similarly, a suspension of XM322-luciferase cells (1×10^4) was inoculated at the left fourth inguinal mammary gland of NOD/SCID mice. We selected out mice with tumor dissemination and the tumor photon signals reached to ~500×10^6 photons/second for the following 20 days intervention.

Microarray analyses of mRNA expression profiles

RNA-Seq and microarray analyses were performed on BCSC transfected with TV-circRGPD6 and si-circRGPD6 for 48 hr. RNA extractions were performed using Trizol. Synthesis of cDNA was performed using the SuperScript Choice System according to manufacturer’s protocol (Invitrogen Life Technologies, Capital Biochip Corporation). Microarrays analyses were performed using Affymetrix Genechip scanner 3000 with Affymetrix Genechip Command Console software. Microarray experiments were conducted according to the manufacturer's instructions. To select the differentially expressed genes, we used threshold values of ≥ 2 and ≤ -2 -fold change and a Benjamini-Hochberg corrected *p* value of 0.05. Gene expressions were normalized by using Log2 transformation and then median-centering was used for the adjustment by the Adjust Data function of Cluster 3.0 software. Data was subsequently analyzed for hierarchical clustering with average linkage (genes which value more than 100 were evaluated). Finally, we performed tree visualization with Java Treeview (Stanford University School of Medicine, Stanford, CA, USA). The results had been submitted to ArrayExpress (accession number E-MTAB-5584, E-MTAB-7556 and E-MTAB-7557).

REFERENCES

1. Lin X, Chen W, Wei F, Zhou BP, Hung MC, Xie X. (2017) POMC maintains tumor-initiating properties of tumor tissue-derived long-term-cultured breast cancer stem cells. Int. J. Cancer *140*, 2517-2525.
2. Lin X, Chen W, Wei F, Zhou BP, Hung MC, Xie X. (2017) Nanoparticle Delivery of miR-34a Eradicates Long-term-cultured Breast Cancer Stem Cells via Targeting C22ORF28 Directly. Theranostics *7*, 4805-4824.
3. Xie X, Xia W, Li Z, Kuo HP, Liu Y, Li Z, et al. (2007) Targeted expression of BikDD eradicates pancreatic tumors in noninvasive imaging models. Cancer Cell *12*, 52-65.
4. Merino D, Whittle J, Vaillant F, Serrano A, Gong JN, Giner G, et al. (2017) Synergistic action of the MCL-1 inhibitor S63845 with current therapies in preclinical models of triple-negative and HER2-amplified breast cancer. Sci. Transl. Med. *9*, 7049-7059.
5. Lang JY, Hsu JL, Meric-Bernstam F, Chang CJ, Wang Q, Bao Y, et al. (2011) BikDD eliminates breast cancer initiating cells and synergizes with lapatinib for breast cancer treatment. Cancer Cell *20*, 341-356.
6. Li L, Xie X, Luo J, Liu M, Xi S, Guo J, et al. (2012) Targeted expression of miR-34a using the T-VISA system suppresses breast cancer cell growth and invasion. Mol. Ther. *20*, 2326-2334.
7. Huang HC, Pigula M, Fang Y, Hasan T. (2018) Immobilization of Photo-Immunoconjugates on Nanoparticles Leads to Enhanced Light-Activated Biological Effects. Small *1*, e1800236.
8. Xie X, Li L, Xiao X, Guo J, Kong Y, Wu M, et al. (2012) Targeted expression of BikDD eliminates breast cancer with virtually no toxicity in noninvasive imaging models. Mol. Cancer Ther. *11*, 1915-1924.
9. Lu Y, Yue Z, Xie J, Wang W, Zhu H, Zhang E, et al. (2018) Micelles with ultralow critical micelle concentration as carriers for drug delivery. Nat. Biomed. Eng. *2*, 318-325.

Supplementary Tables S1-4

Supplementary Table S1. starBase predicts the miRNAs sponging circRGPD6

MiRNA ID	MiRNA Name	Gene ID	Ggene Name	Gene Type	Chromosome	Target Sites
MIMAT0000101	hsa-miR-103a-3p	NM_001037866	RGPD6	circRNA	chr2	8
MIMAT0000104	hsa-miR-107	NM_001037866	RGPD6	circRNA	chr2	8
MIMAT0000423	hsa-miR-125b-5p	NM_001037866	RGPD6	circRNA	chr2	6
MIMAT0000417	hsa-miR-15b-5p	NM_001037866	RGPD6	circRNA	chr2	11
MIMAT0000076	hsa-miR-21-5p	NM_001037866	RGPD6	circRNA	chr2	5
MIMAT0000418	hsa-miR-23b-3p	NM_001037866	RGPD6	circRNA	chr2	9
MIMAT0000080	hsa-miR-24-3p	NM_001037866	RGPD6	circRNA	chr2	9
MIMAT0000083	hsa-miR-26b-5p	NM_001037866	RGPD6	circRNA	chr2	9
MIMAT0000419	hsa-miR-27b-3p	NM_001037866	RGPD6	circRNA	chr2	10
MIMAT0000086	hsa-miR-29a-3p	NM_001037866	RGPD6	circRNA	chr2	8
MIMAT0000100	hsa-miR-29b-3p	NM_001037866	RGPD6	circRNA	chr2	8

Supplementary Table S2. 12 miroRNA expressions were changed following the regulation of circRGPD6 in both MCF-7.SC and XM322

Name of miRNA	Mature sequence
hsa-miR-103a-3p	TCATAGCCCTGTACAATG
hsa-miR-24-3p	CTGTTCCTGCTGAACTGA
hsa-miR-107	TGATAGCCCTGTACAATGCT
hsa-miR-27a-3p	GCGGAACTTAGCCACTG
hsa-miR-125b-5p	TCACAAGTTAGGGTCTC
hsa-miR-27b-3p	GCAGAACTTAGCCACTGT
hsa-miR-15b-5p	TGTAAACCATGATGTGCTGC
hsa-miR-148b-3p	ACAAAGTTCTGTGATGCAC
hsa-miR-26b-5p	ACCTATCCTGAATTACTTGA
hsa-miR-23b-3p	GGTAATCCCTGGCAATG
hsa-miR-29b-3p	AACACTGATTTCAAATGGTGC
hsa-miR-29a-3p	TAACCGATTTCAGATGGTGC

Supplementary Table S3. Thirty-seven co-target genes of miR-26b based on four algorithms (TargetScan, miRanda, TargetMiner and miRWalk)

4 algorithms	37 co-target genes of miR-26b
TargetScan, MIRDB, TargetMiner and miRWalk	As following: ELAVL2, E2F7, RHOQ, PRKCD, SLC38A2, ADAM9, CREBZF, FAM136A, TMCC1, ULK2, PTP4A1, TMEM2, KPNA6, TET3, CXADR, BLOC1S2, ABHD2, ZBTB18, PLOD2, GNA13, TNRC6B, ZNF608, RCOR1, SFXN1, YAF2, HGF, SLC19A2, RCBTB1, PTEN, GTF2A1, ZNF410, USP9X, SACS, CREBRF, REEP4, MAT2A, USP3.

Supplementary Table S4. Clinicopathological features of 165 patients with breast cancer

	Stage I	Stage II	Stage III	Stage IV
Totality	16	58	60	31
Age (years)				
<50	8	35	39	17
≥50	8	23	21	14
Pathogenetic location				
Left breast	8	30	27	15
Right breast	2	28	33	16
Family history of cancer				
Absence	14	56	55	28
Presence	2	2	5	3
Histological type				
Ductal	13	56	59	30
Lobular	3	2	1	1
Pathological grading				
1	4	13	17	3
2	4	18	17	8
3	8	24	19	16
Undifferentiated	0	3	6	3
Not available	0	0	1	1
ER status				
Negative	8	31	44	20
Positive	8	27	16	11
PR status				
Negative	8	30	42	19
Positive	8	28	18	12
Herb2 status				
Negative	14	48	50	17
Positive	2	10	10	14
Triple-negative breast cancer				
Absence	9	45	29	14
Presence	7	13	31	17
p53 status				
Negative	8	30	19	8
Positive	8	28	41	23

Supplementary Figures 1-7

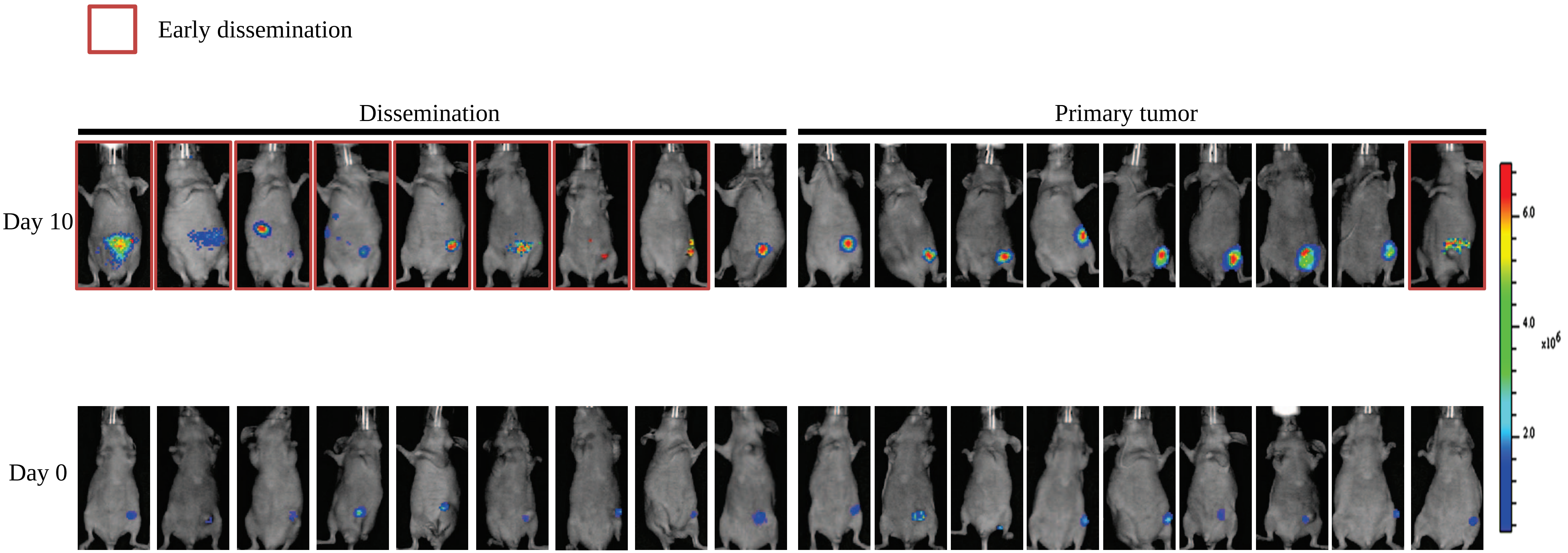

Figure S1. Monitoring dissemination of primary MCF-7-bearing tumor and disseminated MCF-7-bearing tumor in NOD/SCID mice. Mice are imaged for 10 days after implantation when palpable tumors formed.

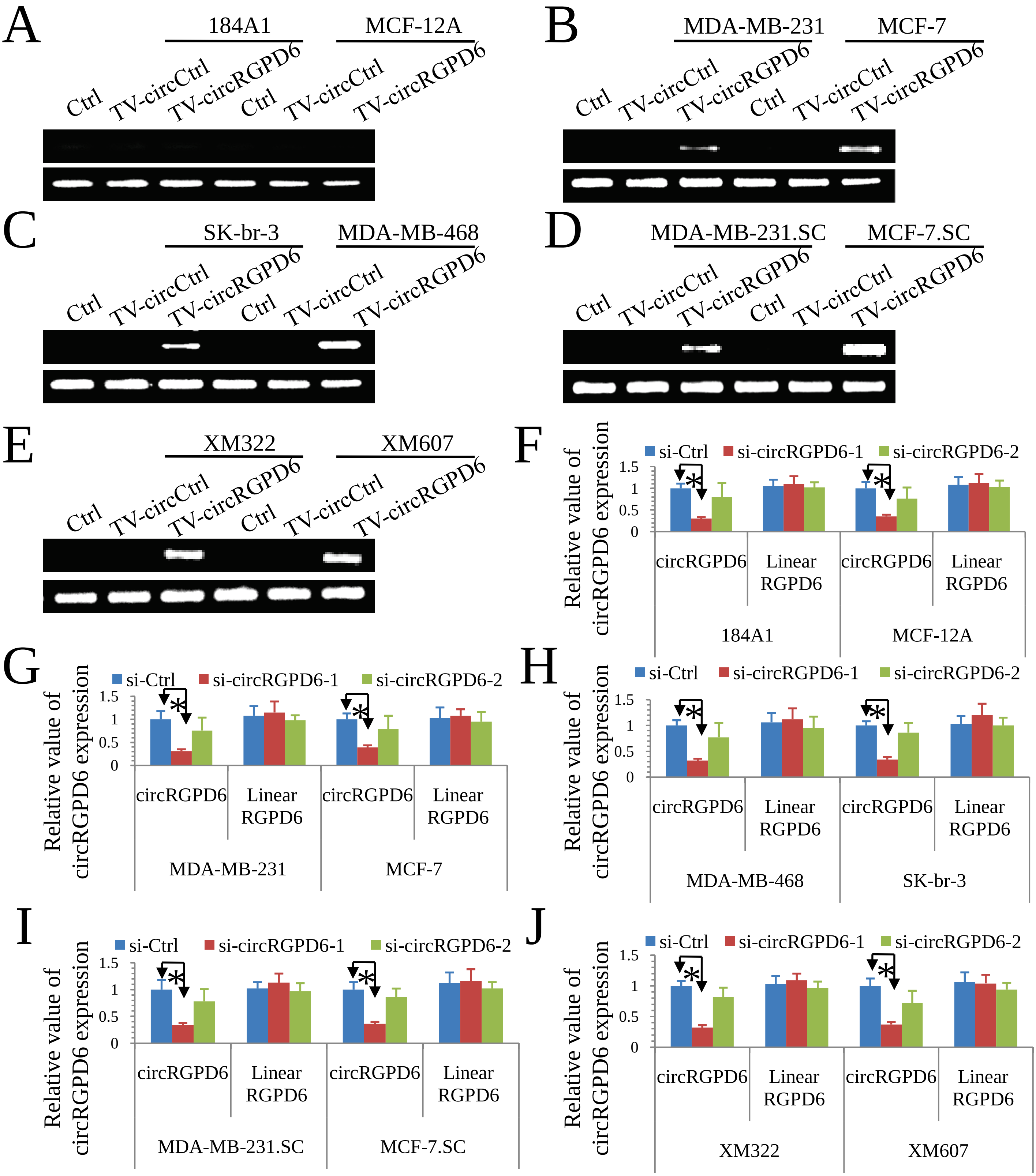

Figure S2. Determination of the regulators of circRGPD6. (A-E) Reverse Transcription-PCR confirmation of circRGPD6 expression in liposomal complex, TV-Ctrl and TV-circRGPD6-transfected breast cells: (A) Healthy mammary epithelial cells: 184A1 and MCF-12A; (B) Breast cancer cells: MDA-MB-231 and MCF-7; (C) Breast cancer cells: SK-br-3 and MDA-MB-468; (D) BCSC lineages derived from breast cancer cells: MDA-MB-231.SC and MCF-7.SC; (E) Tumor tissue-derived BCSC: XM322 and XM607. (F-J) qRT-PCR to verify the circRGPD6 silencing efficiency and rule out the possibility that circ circRGPD6 siRNA might exert effects on the mRNA level of circRGPD6 (linear circRGPD6) in multiple breast cells: (F) 184A1 and MCF-12A; (G) MDA-MB-231 and MCF-7; (H) SK-br-3 and MDA-MB-468; (I) MDA-MB-231.SC and MCF-7.SC; (J) XM322 and XM607. Each experiment was repeated at least in triplicate. * indicates *P* <0.05. Statistical analysis was performed using the paired *t*-test.

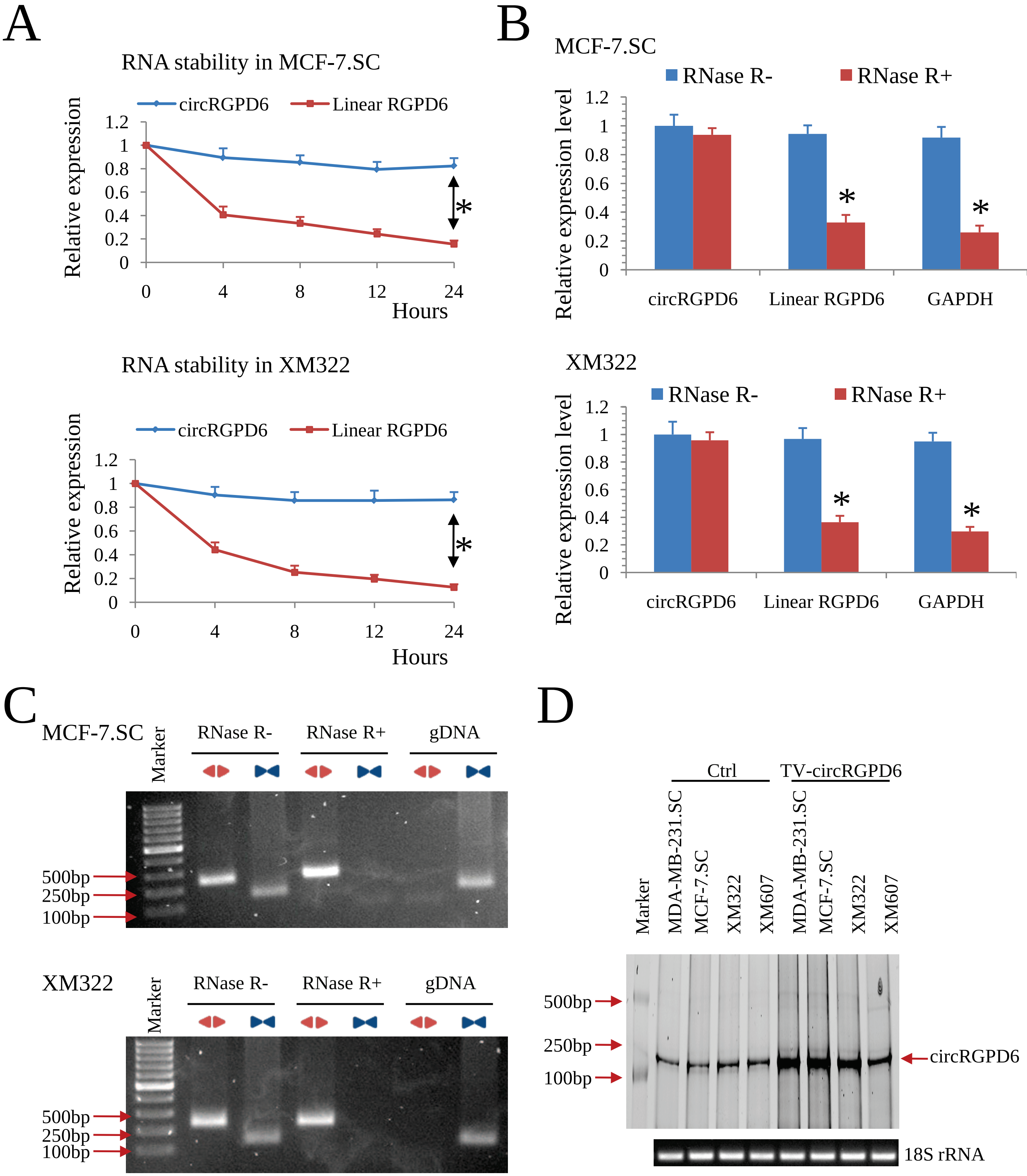

Figure S3. Characteristics of circRGPD6 in BCSC. (A) qRT-PCR for the expression of circRGPD6 and RGPD6 mRNA in both MCF-7.SC and XM322 treated with Actinomycin D, a transcription inhibitor. (B) qRT-PCR assay with specially designed divergent and convergent primers and indicated that circRGPD6, rather than linear RGPD6 or GAPDH, could resist digestion by RNase R. (C) Expression levels of the back-spliced and canonical forms of RGPD6 in the presence or absence of RNase R supplementation in cDNA and gDNA from both MCF-7.SC and XM322 by PCR and an agarose gel electrophoresis assay. (D) Ctrl (empty vector) and TV-circRGPD6 were transfected into BCSC. After 24 hr of transfection, total RNA was treated with RNase-R and subjected to Northern blotting using circRGPD6 junction probes. Each experiment was repeated at least three times. * indicates *P* <0.05. Statistical analysis was performed using the paired *t*-test.

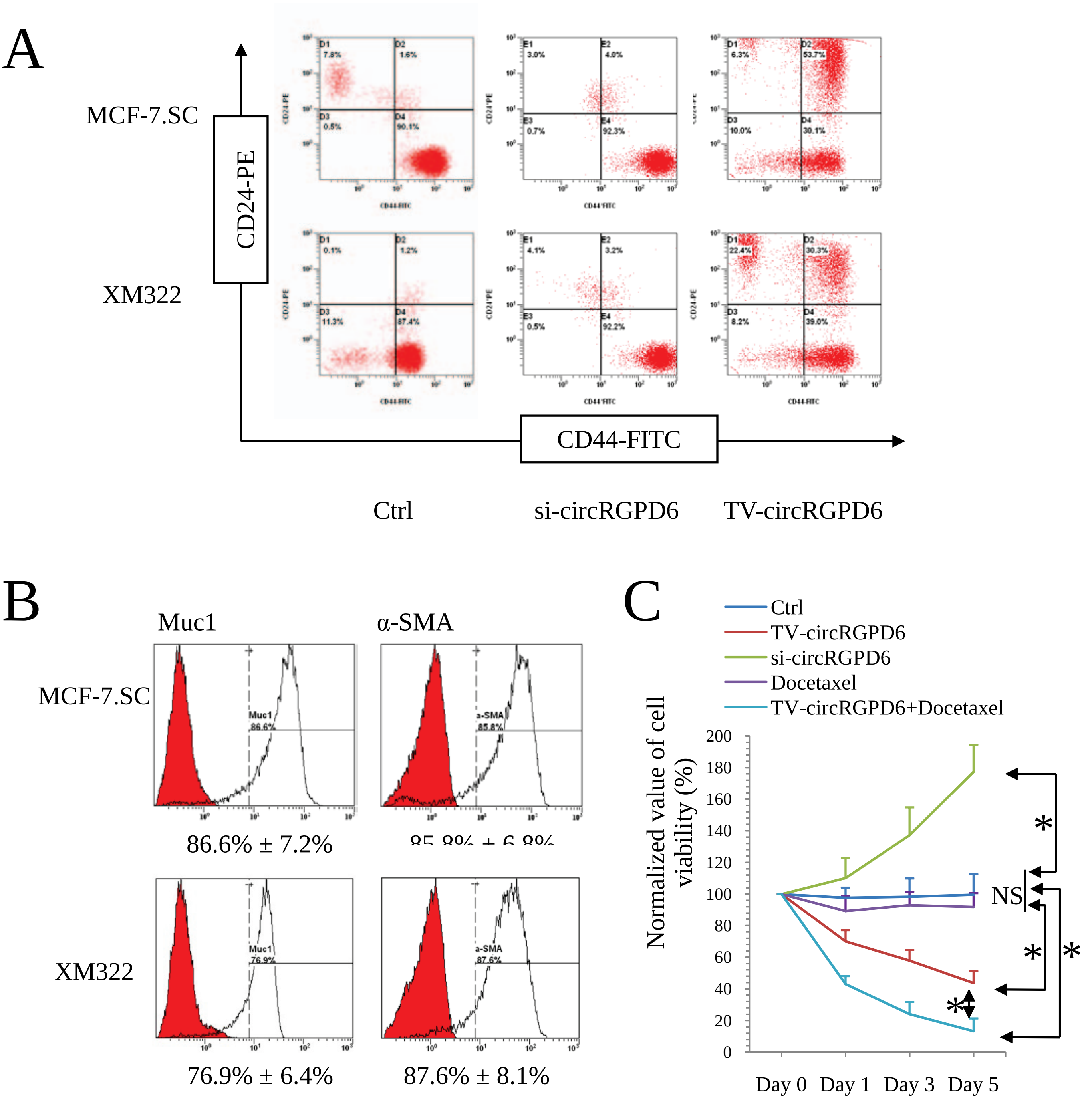

Figure S4. TV-circRGPD6 inhiblts tumor-initiating properties of BCSC *in vitro* (related to Figure 4). (A) Representative images of TV-circRGPD6 robustly decreasing the $CD44^+CD24^-$ subpopulation of MCF-7.SC and XM322. (B) TV-circRGPD6 enhanced the pluripotency in both MCF-7.SC and XM322. After differentiation, TV-circRGPD6 treated BCSC had increased Muc1-positive cells (Muc1-PE) accounted for approximately 80% (left panel) and increased α-SMA-PE positive cells accounted for approximately 85% (right panel). Peaks labeled in red represent isotype control. (C) MTT assays indicated that TV-circRGPD6 synergizes with docetaxel to eradicate XM322. Each experiment was repeated at least three times. * indicates $P < 0.05$; NS: not significant. Statistical analyses were performed using multi-factor analysis of variance (univariate).

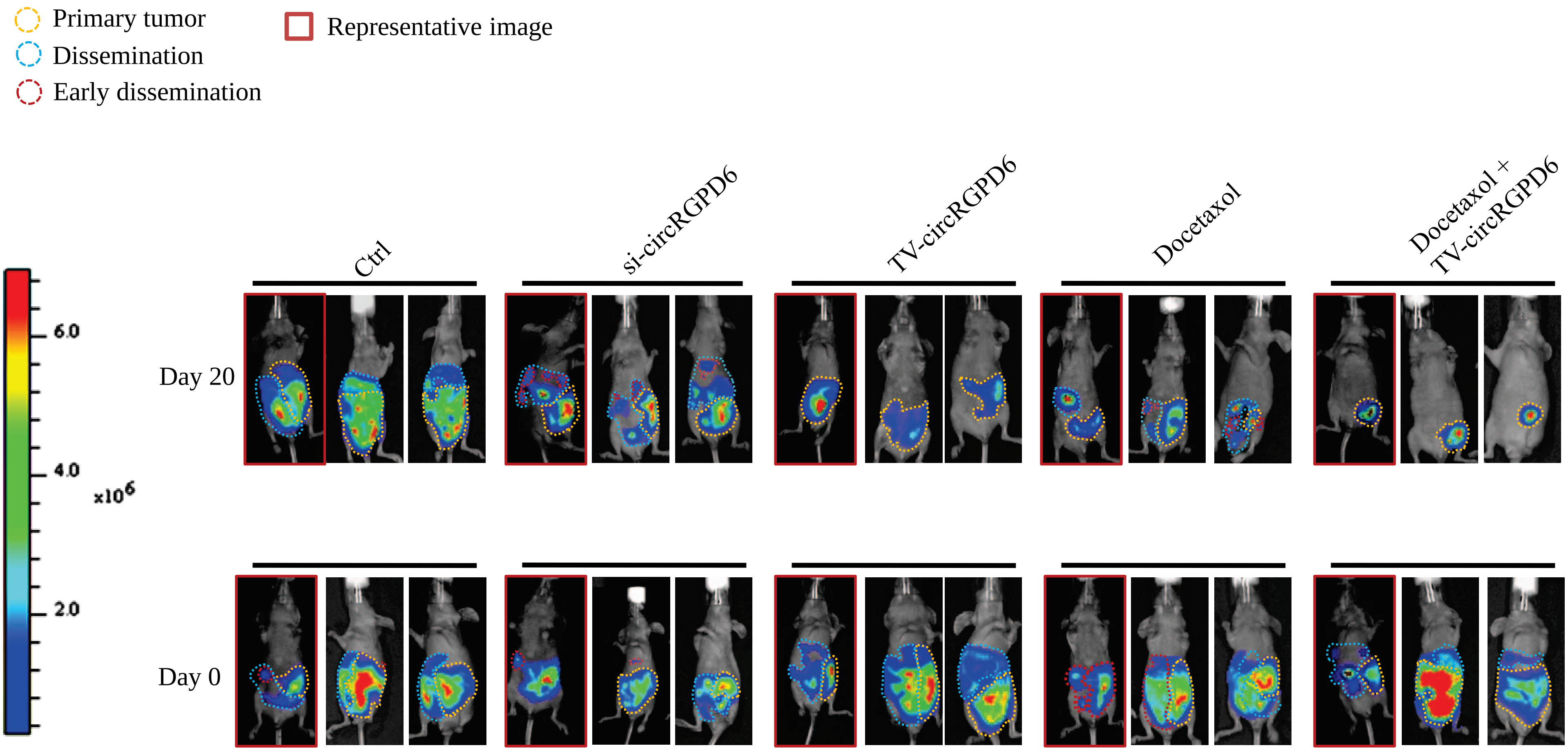

Figure S5. Photon signals of tumors in the XM322-bearing mice with Ctrl, si-circRGPD6, TV-circRGPD6, docetaxol alone, and Docetaxol plus TV-circRGPD6 (3 mice per group).

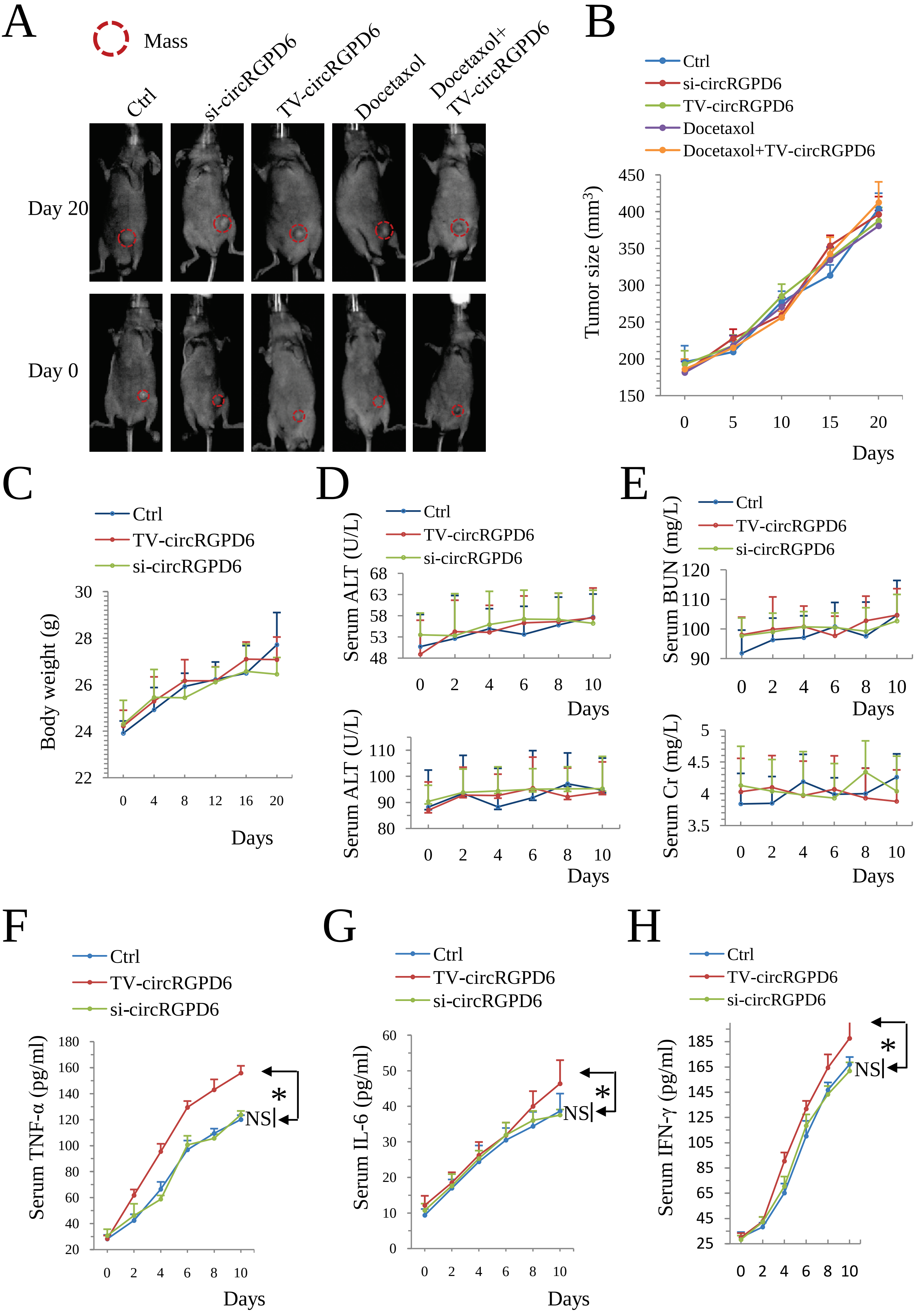
A
Mass
Ctrl
si-circRGPD6
TV-circRGPD6
Docetaxol
Docetaxol+
TV-circRGPD6
Day 20
Day 0
B
Ctrl
si-circRGPD6
TV-circRGPD6
Docetaxol
Docetaxol+TV-circRGPD6
Tumor size (mm^3)
450
400
350
300
250
200
150
0
5
10
15
20
Days
C
Ctrl
TV-circRGPD6
si-circRGPD6
Body weight (g)
30
28
26
24
22
0
4
8
12
16
20
Days
D
Ctrl
TV-circRGPD6
si-circRGPD6
Serum ALT (U/L)
68
63
58
53
48
0
2
4
6
8
10
Days
Serum ALT (U/L)
110
100
90
80
0
2
4
6
8
10
Days
E
Ctrl
TV-circRGPD6
si-circRGPD6
Serum BUN (mg/L)
120
110
100
90
0
2
4
6
8
10
Days
Serum Cr (mg/L)
5
4.5
4
3.5
0
2
4
6
8
10
Days
F
Ctrl
TV-circRGPD6
si-circRGPD6
Serum TNF-α (pg/ml)
180
160
140
120
100
80
60
40
20
*
NS
0
2
4
6
8
10
Days
G
Ctrl
TV-circRGPD6
si-circRGPD6
Serum IL-6 (pg/ml)
60
50
40
30
20
10
0
*
NS
0
2
4
6
8
10
Days
H
Ctrl
TV-circRGPD6
si-circRGPD6
Serum IFN-γ (pg/ml)
185
165
145
125
105
85
65
45
25
*
NS
0
2
4
6
8
10

Figure S6. TV-circRGPD6 treatment for BCSC-bearing mice is well-tolerated *in vivo*. (A-B) Neither TV-circRGPD6 alone nor docetaxel alone plays an inhibitory effect on 184A1-bearing tumors *in vivo* (10 mice per group). Representative images (A) and statistical results (B) of xenografts growing in nude mice for 20 days after injection with 184A1. (C) Body weight of all nude mice in the experiment showed no significant change. (D) Serum ALT (upper panel) and AST (lower panel) of XM322-bearing mice with treatment of Ctrl, TV-circRGPD6 and si-circRGPD6 for 10 days. (E) Serum BUN (upper panel) and Cr (lower panel) of XM322-bearing mice with treatment of Ctrl, TV-circRGPD6 and si-circRGPD6 for 10 days. (F-H) Serum concentrations of TNF-α (F), IL-6 (G) and IFN-γ (H) of XM322-bearing tumors with treatment of Ctrl, TV-circRGPD6 and si-circRGPD6 for 10 days. Each experiment was repeated more than five times. * indicates $P < 0.05$; NS: not significant

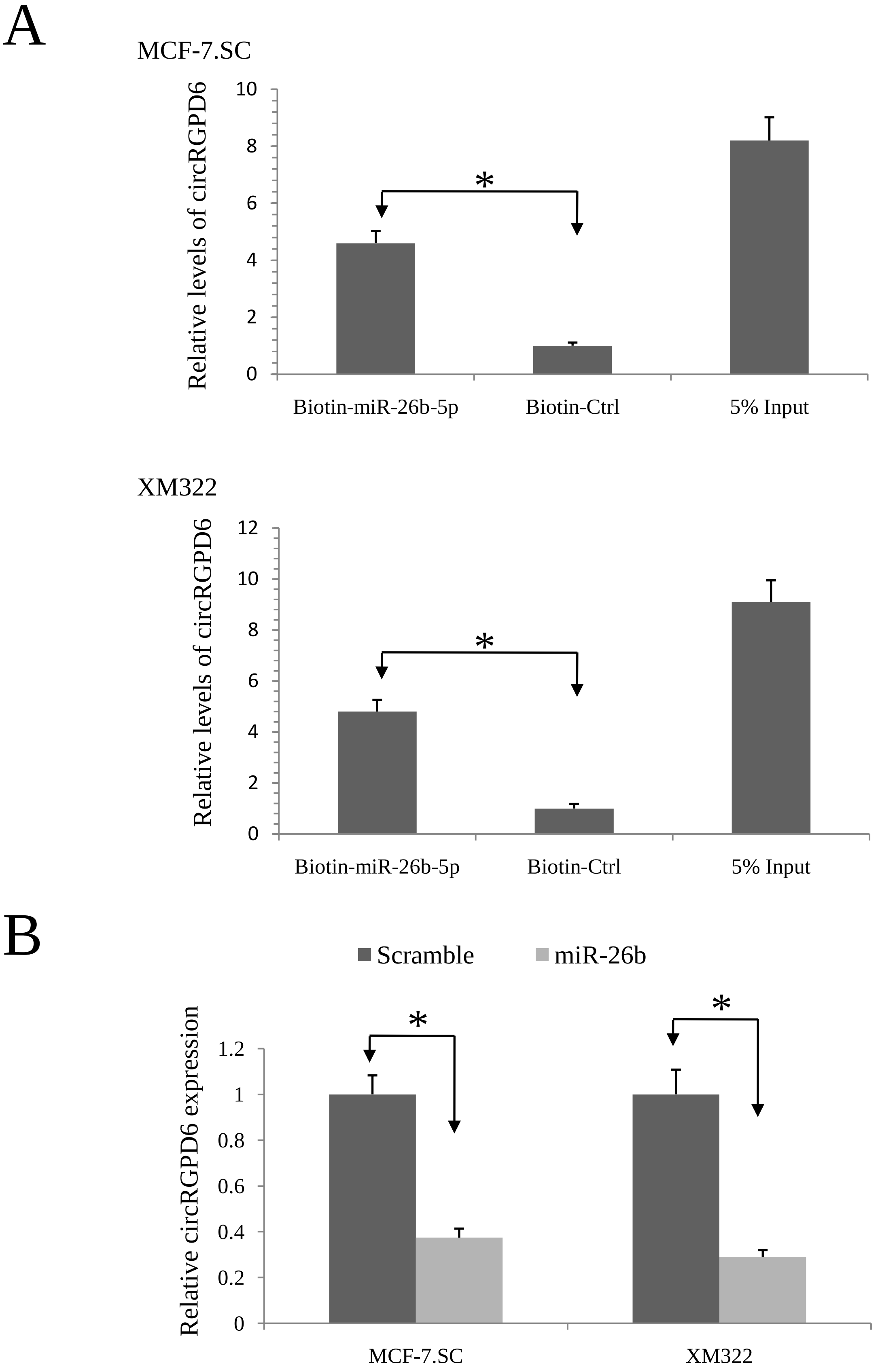

Figure S7. TV-circRGPD6 serves as a miRNA sponge for miR-26b (related to Figure 6). (A) We used a specific biotin-labelled miR-26b-5p probe to successfully capture circRGPD6 compared to the Ctrl group in MCF-7.SC (upper panel) and XM322 (lower panel). (B) qRT-PCR analyses of circRGPD6 expressions following transfection with a scrambled Ctrl, miR-26b mimics in MCF-7.SC and XM322. Statistical analysis was performed using the paired *t*-test.